JGR Oceans

RESEARCH ARTICLE
10.1029/2022JC018577

Influence of Winter Subsurface on the Following Summer Variability in Northern California Current System

Sulagna Ray[1], Nicholas Bond[2,3], Samantha Siedlecki[4], and Albert J. Hermann[2,3]

[1]SAIC at NOAA/NCEP/EMC, College Park, MD, USA, [2]University of Washington, Joint Institute for the Study of the Atmosphere and Ocean, Seattle, WA, USA, [3]NOAA Pacific Marine Environmental Lab (PMEL), Seattle, WA, USA, [4]Department of Marine Sciences, University of Connecticut, Groton, CT, USA

Key Points:

- Northern CCS summer temperatures are more strongly correlated with winter prior subsurface temperatures during ENSO-neutral years
- Changes in isopycnals and currents during ENSO reduce the effects of persistence in the subsurface temperatures found for ENSO-neutral years
- Pre-conditioning of the winter subsurface during ENSO-neutral years is a source of predictability for the following summer temperatures

Correspondence to:
S. Ray,
sulagna.ray@noaa.gov

Citation:
Ray, S., Bond, N., Siedlecki, S., & Hermann, A. J. (2022). Influence of winter subsurface on the following summer variability in Northern California Current System. *Journal of Geophysical Research: Oceans*, *127*, e2022JC018577. https://doi.org/10.1029/2022JC018577

Received 24 FEB 2022
Accepted 7 DEC 2022

Abstract Temperature variations in the North and tropical Pacific contribute to the predictability of temperatures along the 26.4σ isopycnal layer off the Northern California Current System (N-CCS). Monthly temperature variations at this depth in the N-CCS are related to a linear combination of factors, including North Pacific spice anomalies, and the PDO and ENSO climate indices. However, the mechanisms for seasonal predictability of subsurface temperatures, are not well explored. While wind and buoyancy driven deep winter mixing influence subsurface temperatures during the following summer in the deep basin of the North Pacific, a coupled atmosphere-ocean reanalysis (the CFSR) reveals that winter prior surface temperatures explain only 25% of the summer subsurface temperatures in the N-CCS. A heat budget of the intermediate layer between a temporally varying mixed layer and the 26.4σ level is diagnosed here to explore the possible role of oceanic advection in explaining the remaining variance. Warmer waters from the south near the coast drive temperature changes in ENSO-neutral winters, thereby preconditioning temperatures for the following summer. During ENSO winters, isopycnal variations associated with propagating coastal kelvin waves and other sources of heaving, along with anomalous alongshore currents, drive convergence/divergence of the advective fluxes, thereby reducing the local memory of the winter subsurface temperatures. Variations in winter advection could account for almost 36% of the summer subsurface temperature variability in the N-CCS; this exceeds the portion explained by the heat fluxes associated with deep winter mixing.

Plain Language Summary Summer upwelling brings colder waters onto the shelf and signifies the beginning to the highly productive season for fisheries and ecosystems off the Northern California Current System (N-CCS). Along the bottom, many important marine species reside with associated thermal tolerances that have been exceeded during recent warm events. Advanced knowledge of these events on seasonal or longer timescales aids in fisheries management. Understanding processes driving seasonal and interannual variations of subsurface temperature conditions is vital to developing prognostic skill. Regional climate indices, like the Pacific Decadal Oscillation and El Niño and Southern Oscillation (ENSO), are correlated with subsurface temperature variability in the N-CCS, yet the actual drivers of seasonal subsurface temperatures are not well explored. Here we show that summer temperatures are related to the conditions in the winter prior and that the strength of this connection depends on whether or not the winter features an ENSO event. Along-shore currents near the coast during non-ENSO winters are responsible for much of the preconditioning of the subsurface temperatures observed the following summer. During ENSO winters, this preconditioning is weaker, because subsurface variations associated with isopycnal heave and coastally trapped waves, along with changes in poleward currents, influence the subsurface summer temperatures.

1. Introduction

Waters at pycnocline depth along the US west coast exhibit temperature variations and trends that do not necessarily match those near the surface (Alexander et al., 2020; Brickman et al., 2021; Rasmussen et al., 2020; S. Siedlecki, Pilcher, et al., 2021), with consequences for coastal ocean properties such as stratification, oxygen concentration, and acidification (Alexander et al., 2020, 2018; Kwiatkowski et al., 2020; S. A. Siedlecki, Pilcher, et al., 2021). A variety of marine species are known to be sensitive to subsurface ocean conditions of the region including lower-trophic species such as krill (Cimino et al., 2020; Lilly & Ohman, 2021), and higher trophic level species such as Pacific hake (Malick et al., 2020). Thus, a better understanding of the factors controlling physical and biogeochemical conditions of subsurface waters would be useful for management toward maintaining a sustainable and a resilient ecosystem.

Marine Heat Waves (MHW) have recently become prominent in the region (2015, 2018, 2020) with upper ocean heat contents projected to increase (Frölicher et al., 2018; Oliver et al., 2019). The upper ocean warming could lead to advection of warmer and saltier waters along the California Current System (CCS) (Ren & Rudnick, 2021), with impacts on the distribution of marine species (Jacox et al., 2020; Rogers-Bennett & Catton, 2019; Suryan et al., 2021), leading to marine disease outbreaks (Aalto et al., 2020), toxic algal blooms (McCabe et al., 2016; Ryan et al., 2017) and disturbing the highly productive ecosystem in the Northern California Current System (N-CCS) (Peterson et al., 2017; Sanford et al., 2019). Heat budget analysis studies have shown that the MHWs (2015, 2018) along the Pacific Northwest coast are driven by surface warming (Bond et al., 2015; Fumo et al., 2020), or reduced surface winds (Amaya et al., 2020; Fewings & Brown, 2019) or a combination of wind induced downwelling and arrival of coastally trapped waves (CTW)- that deepen the coastal thermocline (Wei et al., 2021). Enhanced role of CTW in skillfully predicting sea surface height of the region (Amaya et al., 2022) could also have implications on thermocline temperatures predictions. On the other hand, the mechanisms responsible for temperature fluctuations at depth have received considerably less attention. Exceptions are presented by Zaba et al. (2020) and Scannell et al. (2020), who emphasized the importance of vertical and poleward advection, and isopycnal heaving, respectively, on subsurface warming. The relative importance of these factors depends on latitude. The variety of potential factors responsible for the subsurface temperature variability in the CCS calls for a robust analysis of seasonal and interannual variations in heat budgets over an extended period including multiple ENSO events.

Winter preconditioning through large-scale atmospheric forcing influences the variation and prediction of biological responses in the CCS (Schroeder et al., 2013). For much of the North Pacific, heat anomalies formed at depths during winter remain trapped the following summer, and then are entrained into the upper mixed layer during the subsequent winter, thus preconditioning the surface ocean in the process known as re-emergence (Alexander et al., 1999). Re-emergence is apparently less important in the CCS along the coast where ENSO teleconnections are more prominent (Byju et al., 2018). Persistence alone has been suggested to be responsible for skillful prediction of bottom temperatures in the N-CCS (Jacox et al., 2020), although it was not selected as a predictor for the monthly subsurface temperature at depth during the period 1979–2017 (Ray et al., 2020). Large-scale climate indices, such as the PDO and NPGO have been used to characterize CCS conditions (Di Lorenzo et al., 2008; Di Lorenzo & Mantua, 2016), but appear to be incomplete for the purpose due to temporal changes in their manifestations and relationships (Litzow et al., 2020). In particular, Ray et al. (2020) found that almost 83% of the variability in temperatures along 26.4σ in the N-CCS is explained by a multivariable linear regression of select predictors, most importantly CTW related to ENSO, and water mass anomalies from North Pacific, as well as the PDO. The present study builds upon Ray et al. (2020) by identifying explicitly the subsurface processes that drive seasonal temperatures at depth in the N-CCS. Such identification of physical drivers of temperatures at depth not only facilitates understanding the sources of seasonal predictability in bottom temperatures, but also paves way for better understanding of processes driving sustained multi-year warming from extreme events such as strong El Niños, and MHWs.

Mixed layer (ML) heat budgets are frequently used to diagnose the physical drivers of near surface temperature variations, but heat budgets are less often used to elucidate the mechanisms responsible for subsurface temperature fluctuations. Zaba et al. (2020) demonstrated that air-sea heat flux and advective cooling drives the seasonal temperature variation, and that anomalous vertical and alongshore advection drives the interannual temperature changes during the $2014-16$ warm event. They utilized an ocean estimate from assimilation of glider observations along lines off the Southern CCS, Argo profiles, satellite observations and XBT profiles over a 3-month window in a subsurface heat budget of fixed layer (100–210 m) in their study. The boundaries of this layer are not necessarily along isopycnals, and hence do not encompass a water mass (of similar density), and a choice of $3-month$ window of assimilation is relatively long toward accounting for the seasonal evolution of important mechanisms. In contrast, our study utilizes monthly outputs of an ocean reanalysis (CFSR) from a global climate model and diagnoses the subsurface heat budget evolution between a temporally varying ML and a deeper 26.4σ level, hence a layer with a density surface as a lower boundary.

Following the method outlined in Ray et al. (2018), the volume-integrated heat budget diagnosed in this study calculates the oceanic advective fluxes across closed lateral boundaries, with reference to the average temperature of the domain at that instant, similar to Chen et al. (2015); Chen et al. (2016) for the Northeast US coastal region. All the advection components (vertical, zonal and meridional) drive the winter subsurface of the N-CCS region on both seasonal and interannual time-scales. Our results indicate the factors in control of the temperature

variability in the region and ultimately its potential predictability. They indicate which terms are most important for accurate diagnosis of temperatures at depth in the region—that is, the terms for which we need accurate predictions as boundary conditions, in order to predict the temperatures at depth in a dynamically down-scaled regional model. They may also provide insights toward optimizing autonomous ocean observation systems, such as underwater gliders that can provide coverage (down to 1,000 m) of subsurface temperature, salinity, pressure, depth-averaged velocity (Rudnick et al., 2017; Schmidt et al., 2019; Testor et al., 2019). In particular, the present study should be useful in specifying the temporal resolution required for observational surveys (Ren & Rudnick, 2021) to adequately monitor these waters from shorter to longer time-scales.

The remainder of the paper is organized as follows: Section 2.1 describes the data; Section 2.2 describes the method of analysis; Section 2.3 describes the heat budget and layer definitions; Section 2.4 provides the motivation behind selecting the layers; Section 3 presents the result of climatological (ENSO-neutral) and composites of El Niño and La Niña heat budget; Section 4 and Section 5 represent discussion and concluding remarks, respectively.

2. Approach

2.1. Data: CFSR Reanalysis 1979–2017

NOAA's Climate Forecast System Reanalysis (CFSR) (Saha et al., 2010) and Operational Analysis assimilates in situ and satellite observations of the atmosphere and ocean into a global, coupled model using the 3DVAR technique, and is used here over the period 1979–2017 for the study. The CFS forecast fields form the boundary conditions for the J-SCOPE forecast system (S. A. Siedlecki et al., 2016), a dynamically downscale regional forecasting system for the N-CCS.

CFSR's resolution ($25 - 50$ km) is not sufficient to resolve the shelf topography off the Washington/Oregon coast. Hence following Ray et al. (2020) we refer to the 26.4σ temperature (which is roughly at the depth of the pycnocline for the North Pacific) averaged in the N-CCS as the temperature at depth. The focus of this study is on the mechanisms controlling its variability using a subsurface heat budget with 26.4σ level as its lower boundary. We note that the pycnocline depth is generally much greater than that of the ML. Since the seasonal cycle of the ML includes substantial deepening in winter, with a possible intrusion into the deeper 26.4σ level, the exchange of heat at the air-sea interface can impact the heat content in the layer of interest, and hence our analysis includes the role of surface heat fluxes.

2.2. Analysis Method

A monthly climatology is constructed for the period between 1979 and 2017 using the heat budget terms that are derived from monthly fields of temperature, salinity and current in CFSR. A total of 10 El Niño and 8 La Niña events occurred between 1979 and 2017 as listed in the CPC website (NOAA, 2022). A threshold of ± 0.5°C for the Oceanic Niño Index (ONI) (Bamston et al., 1997) is used over a 3 months running mean of ERSST.v5 SST anomalies in the Niño 3.4 region to select the El Niño and La Niña years by CPC. We recognize the small sample sizes for describing each kind of event. Anomalies are constructed from climatology and composite analysis of each are performed over the year of event denoted by 0 and the following and preceding years as $+1$ and -1, respectively. We consider the mean seasonal cycle as the composite of ENSO-neutral years. Our analysis of CFSR output includes construction of correlation maps; these maps were used to help highlight regions where similar relationships between two time series motivated further investigation. In particular, correlation maps (as shown in Figure 1) are insufficient from a mechanistic perspective. Additional analysis is required to quantify the specific mechanisms forcing the temperature anomalies. To quantify the role of individual advective fluxes (zonal, vertical, meridional) we assess the relative importance of their mean values in ENSO neutral conditions and similarly in terms of El Niño and La Niña composites. To test whether sequestering of anomalous heat content at depth is important in the N-CCS, we perform a lag correlation of October and January SST to temperature at all depths in N-CCS, following similar method as in Byju et al. (2018).

Ekman transport driven coastal upwelling/downwelling dominates to depths where winds have a strong influence on the upper ocean, but geostrophic currents driven transport has been shown to be not only significant at depth, but also within the ML (Ding et al., 2021; Zaba et al., 2020). We do not decompose currents into geostrophic and

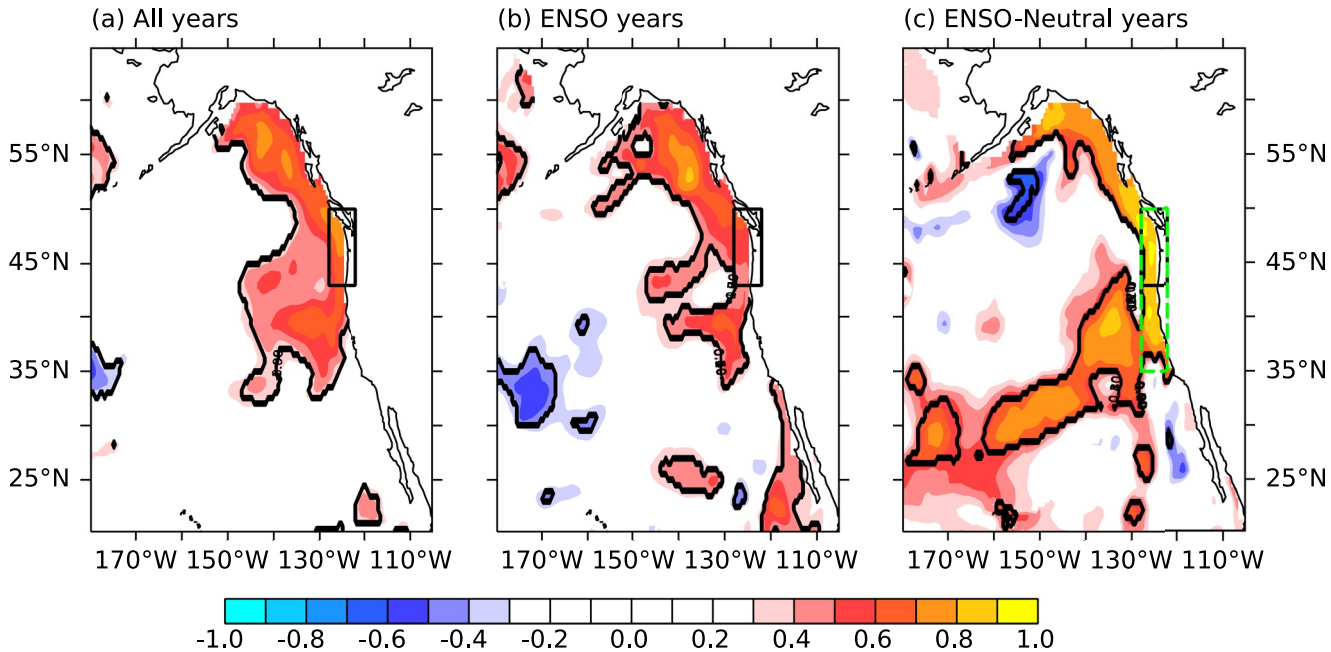

Figure 1. Correlations of May-June-July (MJJ) averaged summer N-CCS temperature at depth to prior October-November-December (OND) averaged temperature along 26.4σ for (a) All years; (b) ENSO years (18); and (c) ENSO-Neutral years (12). 90% significant correlations are shown in bold black contour. The N-CCS domain is shown in a black box. The ESN domain in shown in a green box in (c).

ageostrophic components, however vertical cross-sections of currents are used to illustrate how the flow within the wind-driven upper ML compare with that below, that is, the intermediate layer that is the focus of the present study.

2.3. Subsurface Heat Budget

Heat budgets are evaluated for a region spanning 128°W–122°W; 35°N–50°N which includes the N-CCS (128°W–122°W; 40°N–50°N) domain as well as waters extending a region bit south; here this region is given the name Extended South N-CCS (ESN)—as depicted in Figure 1. The heat budgets include terms for the surface heat flux, shortwave penetration, advection, and entrainment (following on Equation 1 in Ray et al. (2018)) as follows

$$\partial_t T_D = \frac{Q_{\text{sfc}} - Q_{\text{pen}}}{\rho_0 C_p V_D} + \langle \text{advection} \rangle + \langle \text{entrainment} \rangle + \langle \text{residual} \rangle \tag{1}$$

where ∂_i indicates a partial derivative in the i-direction, T is the grid cell-mean temperature, $\rho_0 = 1{,}035$ kg m^{-3} is a constant seawater reference potential density, $C_p \approx 3{,}992$ J kg^{-1} K^{-1} is the specific heat capacity of seawater, $\langle\ \rangle$ denotes a volume average over D covering 128°W–122°W; 35°N–50°N; $T_D = \langle T \rangle$, V_D is the volume of D, Q_{sfc} is the (positive downward) horizontally-averaged net surface heat flux, Q_{pen} is the (positive downward) horizontally-averaged penetrative solar flux at the layer base. The vertical distribution of this incoming solar flux is based on an assumption of exponential attenuation with depth as in Zaba et al. (2020). A water type Jerlov I is used here where 58% of the shortwave attenuates with an e-folding time-scale of 0.35 m and 42% with an e-folding time-scale of 23 m (Paulson & Simpson, 1977). Additional processes are denoted by "residual" that includes vertical mixing, sub-grid scale lateral mixing, and sub-mesoscale mixing, among which vertical mixing plays an important role in the upper ocean. "Advection" denotes the temperature tendency due to advection and the volume-averaged advective tendency is represented as

$$\langle \text{advection} \rangle = -\frac{1}{V_D} \int_{S_D} (\mathbf{u} \cdot \mathbf{n})(T - T_D)\, dS \tag{2}$$

where $\mathbf{u} = (u, v, w)$ is the three-dimensional current velocity, S_D is the bounding surface of D, $\mathbf{n}$ is the outward unit normal vector along S_D, and $T-T_D$ is the temperature anomaly at the boundary relative to the domain average. The total advection thus calculated in terms of an integral of advective fluxes of "relative temperature" over a bounding surface allows a direct measure of the directional heating/cooling due to external influences at each face of the domain D. This is in contrast to advective-form volume integral that includes internal redistribution of temperature within the volume. The difference lies in the directional decomposition and interpretation of the advective components –which is an important aspect of this study. "entrainment" denotes the temperature tendency due to changes in layer depth and following Appendix A in Ray et al. (2018) is represented as

$$\langle \text{entrainment} \rangle = \frac{1}{V_D} \iint_{S_{-h}} (T_{-h} - T_D)\, \partial_t h \;\; dx \;\; dy \tag{3}$$

where h is the layer depth that evolves in time and T_{-h} is the temperature at the base of the layer. Thus entrainment due to a thickening surface layer ($\partial_t h > 0$) tends to *cool* the layer, by annexing cool deep water. Conversely, a negative "entrainment" ("detrainment") due to a thinning surface layer ($\partial_t h < 0$) tends to *warm* the layer as a whole, by excluding cool deep water. This method of calculating the advection and detrainment and other budget terms computes the exact temperature tendency and closes the budget. Compared to diurnally varying fields, monthly fields are restricted to accounting for only the gross effects of entrainment. It is important to emphasize that "entrainment" as defined here represents vertical fluxes of heat content into/out of a generally time-variable volume of fluid. The vertical boundary h may change not only due to explicit vertical turbulent mixing ("turbulent entrainment"), but also due to heating by solar radiation, surface heat flux, and horizontal advection. It is neither a material surface (representing water parcels followed through time), nor a fixed depth in space. The time-varying boundary h could be designed to represent any number of properties, such as the depth of the ML or the depth of a particular isopycnal at that moment in time (as utilized in this study). Stated another way: one may choose any particular fluid volume—such as the volume between the instantaneous ML depth and an instantaneous subsurface isopycnal in a fixed horizontal region—and calculate the time-varying heat fluxes in and out of that fluid volume. Specifically, Equations 1–3 quantify the flux terms for a volume spanning between the surface and a time-varying depth h; these are ultimately used in this study to quantify the heat budget terms for our time-variable subsurface fluid volume between the ML and a deeper isopycnal.

Using monthly data fields from CFSR for the period of 1979–2017, we calculate the heat budget for two layers (a) HB_{ML}: h as the depth of the MLML, that is, at which the potential density referenced to the surface density reaches a critical difference of $\Delta\sigma = 0.125$ kg m^{-3}, and (b) $HB_{26.4\sigma}$: h as the depth of 26.4σ isopycnal. Both these layers vary through time, hence we keep a track of inputs and outputs to a time-varying volume of subsurface water. We focus on the heating of the intermediate layer between (a) and (b), specifically $HB_{26.4\sigma-ML} \equiv HB_{26.4\sigma} - HB_{ML}$, whose details are provided in Appendix A. It bears emphasizing that we are not calculating the exact heat budget of the intermediate layer, but rather estimating it from the heat budgets of the two layers as mentioned above. We acknowledge that as the isopycnal heaves adiabatically, a Lagrangian advection of the moving surface would be more numerically precise than splitting across two different terms—Eulerian advection (related to w) plus entrainment term (related to $\partial_t h$), as above. However, as the vertical velocity (w), layer thickness (h), and change in temperature with depth ($T_{-h} - T_D$) are all calculated at the same time scale (monthly) and depth, the heat flux associated with the Lagrangian advection is close to the sum of the heat fluxes associated with vertical advection and entrainment fluxes on monthly time-scales.

In the present application, the residual in our heat budget consists of parametrized vertical mixing and lateral mixing, and other subgrid-scale and sub-mesoscale processes not resolved by the CFSR. The residual also includes the innovation terms that come from the ocean reanalysis due to assimilation of observed temperatures, and which are rarely stored. The adjusted temperature tendency due to the innovation terms could be quite large and substantially increase the residual if not accounted for in the budget (Zaba et al., 2020). Hence, we do not expect to have a perfect closure in a monthly heat budget, but the residual should at least account for the direction of the unresolved, additional heating or cooling. To test the assumption, we examined the effects of modeled mesoscale eddies and other sub-monthly processes in terms of closure of the heat budget for the intermediate layer using higher temporal resolution fields (daily values) from the CFSR for the year of 1979. The resulting time series of the heat budget shows an excess heating in the residual indicating a missing heating term possibly from vertical diffusive heat flux convergence below the ML. Within this intermediate layer, due to minimal

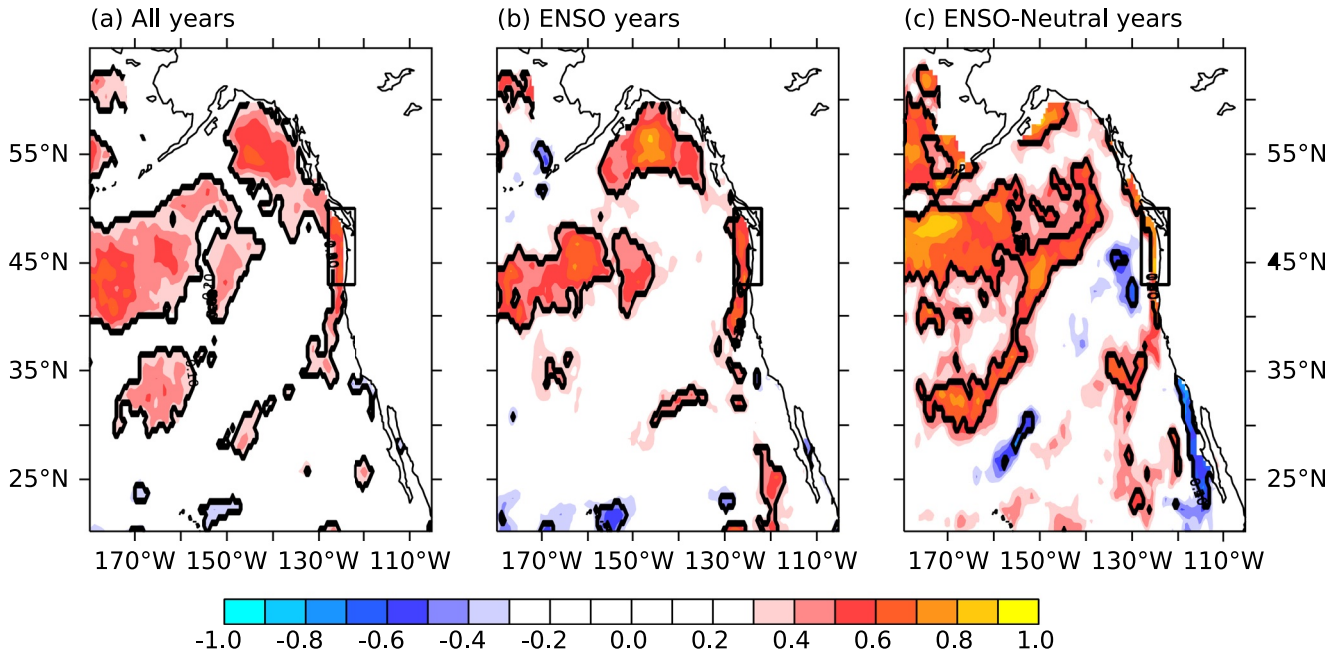

Figure 2. Correlation of MJJ averaged temperature anomaly along 26.4σ isopycnal to prior OND averaged SST anomaly for (a) All years, (c) ENSO years, and (d) Neutral years. 90% significant correlations are shown in bold black contour. The N-CCS domain is shown in a black box.

heating from surface fluxes, the total heating is driven by advection, entrainment, and the processes included in the residual term (Figure A1).

2.4. Motivation for the Subsurface Heat Budget

Correlation maps between the temperatures at depth late in the calendar year with those in the following summer, during both ENSO and ENSO-Neutral years, are shown in Figure 1. The values of these correlations are significant at the 90% confidence level along the Pacific Northwest coast north to the Gulf of Alaska extending westward off-shore (Figure 1a). During ENSO years these correlations are confined closer to the coast (Figure 1b), and during ENSO-Neutral years the correlation strengthens and extends southwestward from the coast into the subtropical central Pacific (Figure 1c). CTW are known to dominate along the US West coast during ENSO events (Jacox et al., 2020). Changes in isopycnal depths would reflect on the deepening/shoaling of the 26.4σ layer along the coast, and could indicate the cumulative effect of downwelling/upwelling CTW or other sources of isopycnal displacement. These ENSO correlations are stronger during La Niña years than during El Niño years (not shown). The correlation patterns do not change materially using 200–250 m averaged temperature instead of temperature along 26.4σ (26.4σ varies between 200 and 280 m) (not shown). Hence we focus on identifying the drivers of winter temperatures at depth seasonally and during El Niño and La Niña years.

Ray et al. (2020) identified that in addition to the atmospheric forcing, subsurface processes below the mixed layer influence SST in the N-CCS during fall/winter months. Winter surface heat fluxes are negatively correlated to SST, which is consistent with the idea that when the SST is warm, surface heat fluxes tend to result in an anomalous heat flux out of the ocean, and vice versa (not shown). Strong positive correlations of fall to winter SST (OND averaged SST anomaly) to the following summer temperature at depth indeed reveals the footprint of deep winter mixing down to the 26.4σ level (Figure 2) consistent with the re-emergence mechanism (Alexander et al., 1999; Byju et al., 2018). While we computed reemergence according to Byju et al. (2018), because our focus is on subsurface regions of the ocean, we will refer to the contribution of reemergence retained in the subsurface as "memory". The weak correlations indicate that deep winter mixing is not very effective in influencing the temperatures down to the 26.4σ level, which possibly indicates a highly stratified ocean suppressing upper ocean mixing. More specifically, the correlations are weak and are confined close to the coast during ENSO years (Figure 2b), and especially in ENSO neutral years (Figure 2c). To test the memory of the subsurface as in Byju et al. (2018), lag correlations of October, November, and December SST anomaly to temperatures at all depths

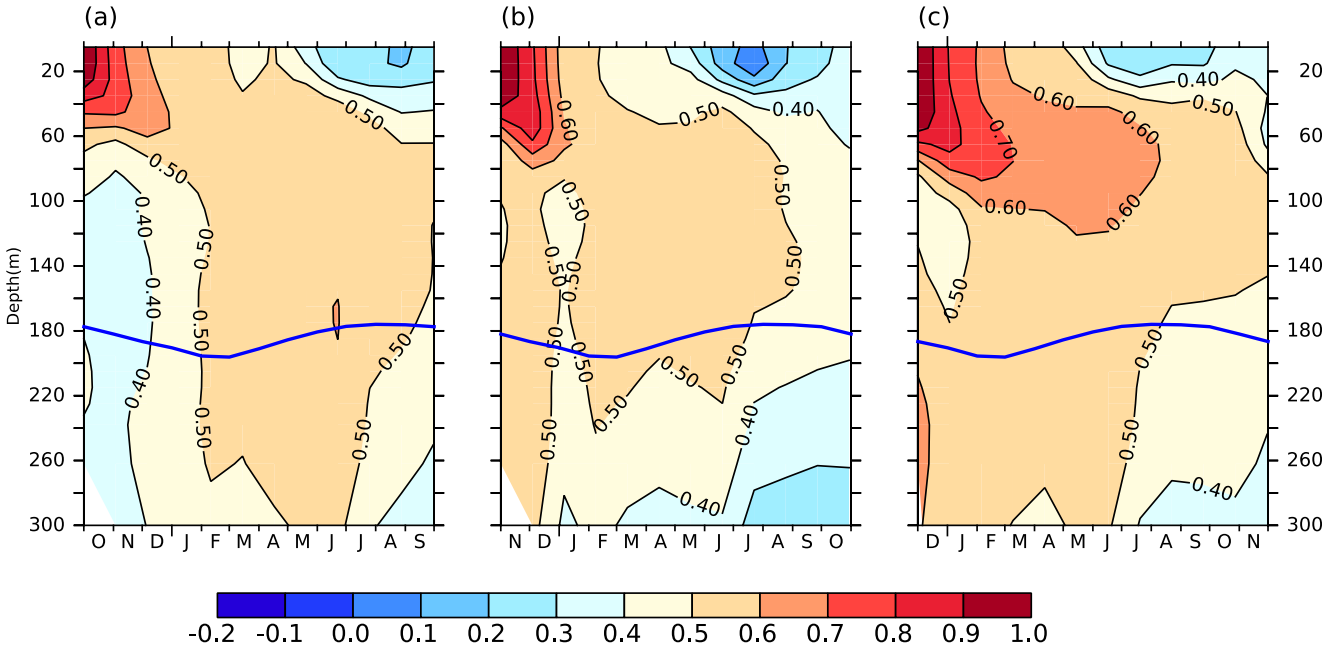

Figure 3. Lag correlation of N-CCS domain averaged SST anomaly in (a) October, (b) November, and (c) December to temperature at depths averaged in the same domain. Overlaid by the N-CCS averaged depth of the 26.4σ isopycnal layer in blue.

averaged within the N-CCS are shown in Figure 3. Correlations to October SST greater than 0.4 penetrate below 100 m at a lag of 2 months, but correlations greater than 0.6 are confined only to the upper 80 m for 2 months. Correlations exceeding 0.6 emerge deeper (below 100 m) from November to December within a month. Larger correlations in June shoal but persist between 40 and 140 m in the subsurface for several consecutive months, and do not re-emerge at the surface. In summary, subsurface processes other than those associated with re-emergence are apparently responsible for somewhere between 64% and 84% of the temperature variability at depth.

3. Results

We present the seasonal cycle (ENSO-neutral) of the ESN heat budget in this section, followed by composites during periods of El Niño and La Niña. The climatological and interannual (anomaly) evolution of the heat budget terms, centered on the winter months, shows the balance of solar penetration and oceanic advection, with mixing and other subgrid-scale processes represented by the residual. The El Niño and La Niña composites of heat budget anomalies start from summer of the ongoing year (0) until the summer of the following year (+1). The results display balance of the various terms in each month, as well as the changes from 1 month to the other.

3.1. Seasonality (ENSO-Neutral) in Subsurface Heat Budget

The seasonal cycle of the heat budget terms for each month from June to May are shown in Figure 4a. The subsurface heats between June and November, undergoes a relatively small change in heat content during the winter months of December through February, and then loses heat from March through May. The temperature tendency is mainly a balance between the cooling from advective fluxes (advection in Figure 4a), and heating from surface fluxes (Qsfc-Qpen in Figure 4a) and residual (residual in Figure 4a). The entrainment term is of negligible magnitude. The residual heating is relatively large in summer (when the ML is shallow, the intermediate layer is thicker, and upwelling is happening in the region), but minimal in winter months between October and February (when the ML is deeper, and the intermediate layer is thinner). From March onwards with the gradual shoaling of ML and thickening of the intermediate layer (Figure A1), the residual heating increases, but works against a subsurface cooling, which is instead dominated by advective cooling. Finally, from June onwards the large residual heating drive a warming of the subsurface. The turbulent vertical diffusive heat fluxes cool the ML, and represent a source of heat for the subsurface (Ray et al., 2018; Zaba et al., 2020). With the vertical diffusive

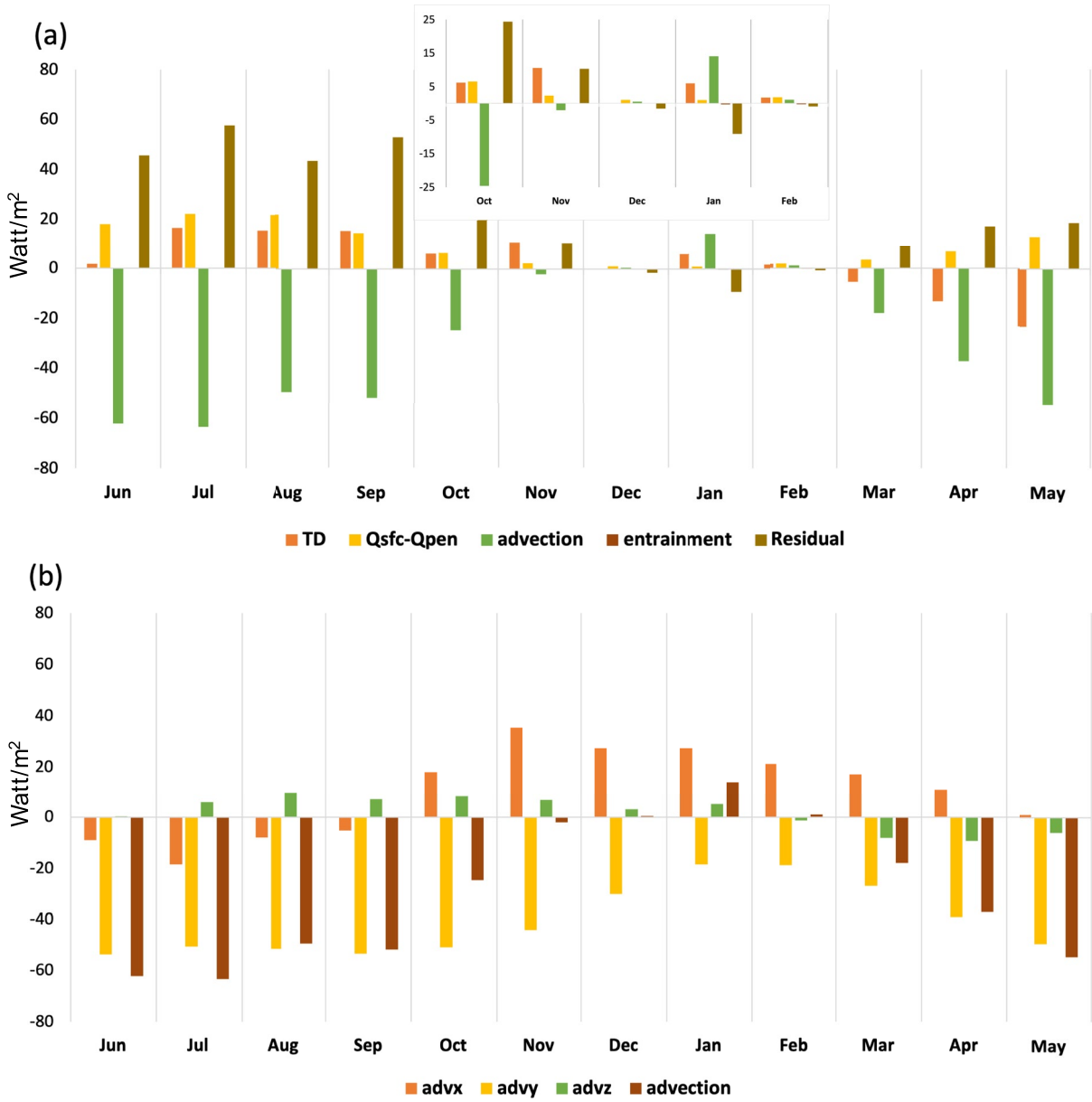

Figure 4. ENSO neutral evolution of ESN subsurface heat budget. Climatology of (a) monthly heat budget terms—total heat (TD~ $T_{D_{26.4\sigma-ML}}$), surface flux heating (Qsfc-Qpen~ $Q_{sfc_{26.4\sigma-ML}} - Q_{pen_{26.4\sigma-ML}}$), heating from advection (advection~$advection_{26.4\sigma-ML}$), entrainment (entrainment~$entrainment_{26.4\sigma-ML}$) and the Residual (Residual~$Residual_{26.4\sigma-ML}$). The relatively small changes in heat content are enlarged to highlight for the months of October-February in the inlet. Also shown are the (b) directional components of advection—zonal (advx~$adv_{26.4\sigma-ML}$), meridional (advy~$adv_{26.4\sigma-ML}$), and vertical (advz~$advz_{26.4\sigma-ML}$). The details of each term is in Appendix A. All terms are in W/m^2. Data used is for the period 1979–2017 from CFSR reanalysis.

heat flux being part of the residual, the residual heating in the intermediate layer is large in summer months. This source of subsurface heating, is countered by the cooling due to advection, especially during June through September. The residual fluxes play a minor role from November through March in the overall heat content. As an example, although the residual heating is relatively large in October and November, the small increase in the subsurface heat content at this time of the year is due in part to a reduction in advective cooling. The relatively small increase in heat content from December to February is primarily driven by advection.

The directional components of the heating due to advection: zonal, meridional, vertical, and total, are shown in Figure 4b. These monthly averages reveal the role of the meridional component in driving the seasonal cycle in the advective cooling, particularly in summer. During winter, the reduced advective cooling is essentially a balance

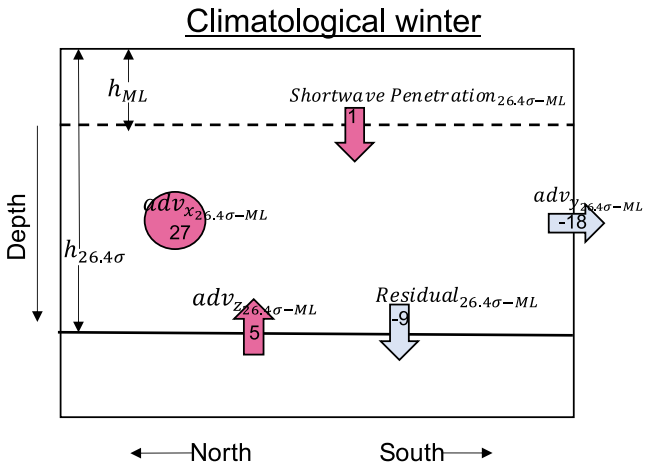

Figure 5. Schematic representation of the dominant fluxes in ESN $HB_{26.4\sigma-ML}$ during ENSO-neutral years. A two-dimensional (yz-plane) figure representing the dominant convergence and divergence of fluxes into $HB_{26.4\sigma-ML}$ in January. The fluxes shown for $HB_{26.4\sigma-ML}$ is estimated for the depth of the layer between $h_{26.4\sigma}$ (26.4σ isopycnal depth) and h_{ML} (mixed layer depth). The numbers represent the average value in W/m^2 following Figure 4. The converging fluxes drives heating in $HB_{26.4\sigma-ML}$ are in red and diverging fluxes driving cooling are in blue and are represented by the direction of the arrows. The schematic is visualized from the western boundary of the ESN box, thus $adv_{x_{26.4\sigma-ML}}$ is directed inward and a heating term.

between an increased heating from the zonal component and a decreased cooling from the meridional component. However, the gradual decrease in cooling from the meridional component seems to play a major role in the presence of a relatively consistent heating from the zonal and vertical components in driving small changes in advective heating through February. A schematic representation of the dominant fluxes heating/cooling the intermediate layer in peak climatological winter is demonstrated in Figure 5. In January, advection drives the heating (14 W/m^2) of the intermediate layer. It is the time of the year when the poleward California Undercurrent (CUC) strengthens (downwelling season, Figure A2), bringing in warmer waters in the intermediate layer from the south, along the deepened 26.4σ layer (Figure A1). The downwelling season also includes heating from the zonal convergence of fluxes. In February, as the 26.4σ layer starts to shoal, the vertical advective flux convergence decreases, driving a net decrease in advection driven heating (1.1 W/m^2) of the intermediate layer. From a climatological perspective, the downwelling season ends in March, as does the zonal flux convergence (reduced zonal advective heating) and meridional component resumes dominating the cooling due to advection from March onwards. In summary, while the meridional component of advection is the primary advective cooling term during most of the year, the winter (November through February) downwelling of the isopycnals near the 26.4σ level and appearance of a poleward flow of warmer waters in the vicinity of the coast (Figure A2a,A2b,A2c), serves to reduce the cooling from the meridional component of advection for the ESN-volume as a whole.

3.2. Composite of Subsurface Heat Budget Anomaly

3.2.1. El Niño Evolution

A composite of El Niño events for the period-1979–2017 (Figure 6) shows that advection drives the anomalous heating of the subsurface in winter months. From August (0) to April (+1), the subsurface remains warmer than during ENSO-neutral years, except for a relatively short cool period in October (0), November (0). The anomalous heating peaks from December (0)-January (+1) (9 − 23 W/m^2) when the intermediate layer is thicker than in ENSO-neutral years, mostly due to a deeper bottom level (26.4σ, by 15 m) (Figure A1). This was expected as the downwelling CTW during El Niño typically arrive around this time and serve to deepen the isopycnals close to coast (Figure A2). The anomalous heating of the intermediate layer gradually turns to cooling by May (+1). With shortwave fluxes playing a negligible role in the thicker intermediate layer, advective fluxes drive the anomalous heating during El Niño. The heating due to the residual closely resembles that in the ENSO-neutral case but it does produce slightly greater cooling of the layer between November (0)-January (+1), thereby countering the warming from advection (Figure A4). Advection drives the total heating from November (0) onwards with a maximum heating occurring in January (+1) (30 W/m^2).

Decomposing the anomalous advection into its directional components shows that all components tend to work together to drive the anomalous advective heating between June (0) and February (+1) (Figure 6). An exception is represented by the months of October (0), and November (0) when the zonal component of the advective fluxes acts to cool the intermediate layer in association with a zonal recirculation centered at 42°N (Figure A3). The meridional component shows an increased warming from October (0) onwards, with a maximum value in January (+1) and a reversal to cooling in March (+1). This coincides with strengthening of anomalous poleward flow via the California Undercurrent (CUC) that starts in October (0) and peaks in December (0)-January (+1) (Figure A2). The strengthened CUC brings in warmer waters from south to heat the intermediate layer during the peak of the event, as found by Zaba et al. (2020) for a single El Niño event—2014/15 in their study but in a 100 − 210 m fixed depth integrated heat budget. The advective cooling via zonal recirculation in October (0) is rapidly overcome by advection of warmer waters from southern boundary and additional warming from vertical component in the following months. The converging zonal advective fluxes from the western boundary also heat the intermediate layer from December (0) to February (+1). An increase in heating from the vertical advective

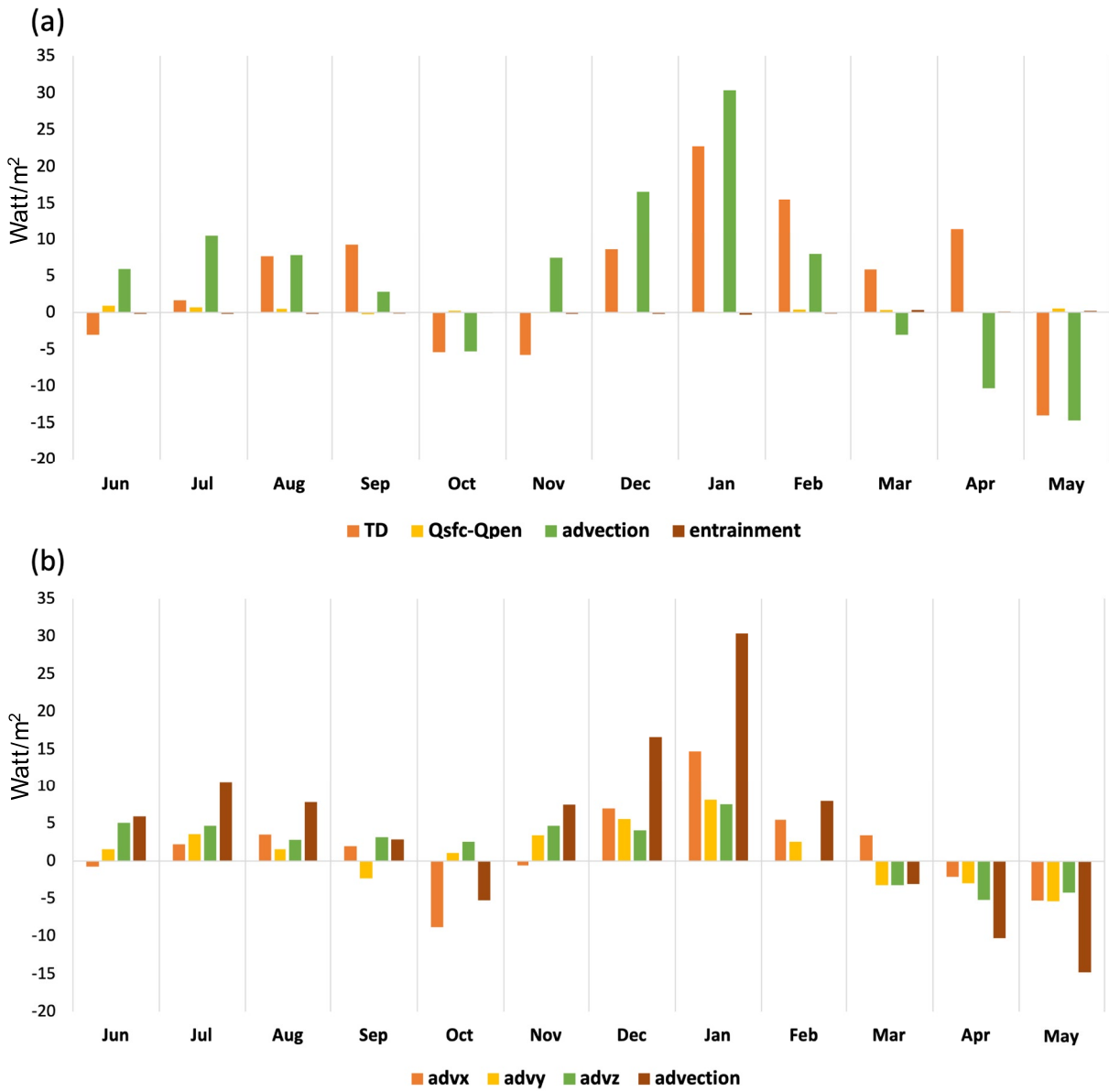

Figure 6. El Niño composite of ESN subsurface heat budget. As in Figure 4, but for composite of 10 El Niño anomalies (removing the climatology) for the period 1979 – 2017 from CFSR reanalysis. Composite evolution of the heat budget anomalies are shown from June (0) to May (+1) centered on the peak winter months. All terms are in W/m^2.

fluxes in the ML to the intermediate layer below ML, along with convergence in the zonal advective fluxes in the ML (not shown) suggests downwelling driven convergence in the intermediate layer, in particular along the coast, which is consistent with the southerly wind anomalies typical of El Niño winters. The downwelling motion extends from the surface to the 26.4σ level in November (0)–December (0), increasing the contribution of the vertical advection to the heating of the intermediate layer with subsequent decreases beyond January (+1). The 26.4σ layer also deepens during this period from October (0) to February (+1) by 20 m (Figure A1) indicating either the passing of downwelling CTWs, which have both remote origins in the equatorial Pacific (Ray et al., 2020) and are locally generated (Jacox et al., 2020), or simply ENSO related changes in isopycnal heaving (Turi et al., 2018). The downwelling of the 26.4σ layer facilitates vertical and zonal advective flux convergence in the intermediate layer and also include depths at which poleward moving CUC brings in warmer waters from the south (Figure 8a). Thus we see that a mix of advective components leads to warming of the intermediate layer during El Niño winters.

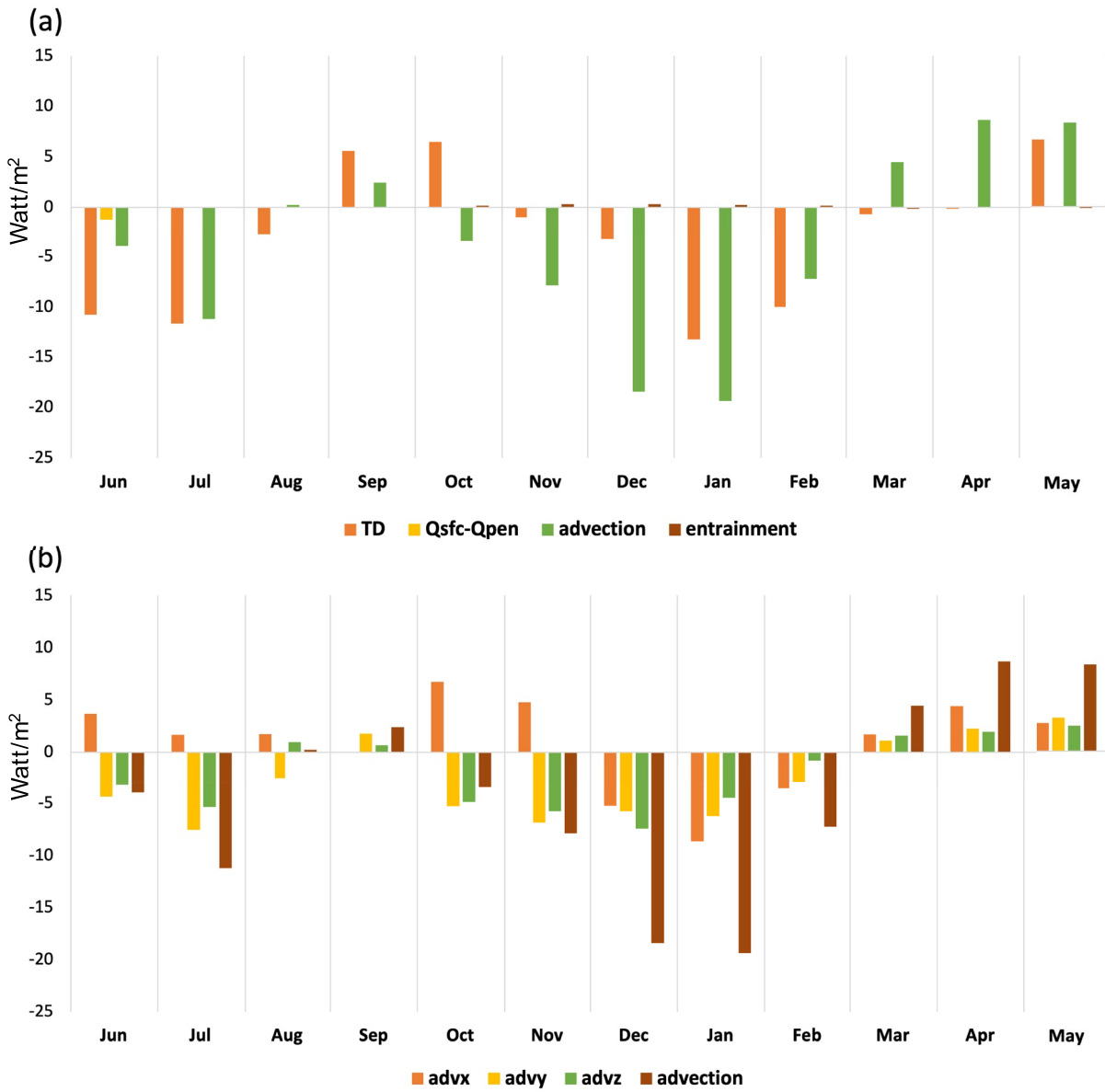

Figure 7. La Niña composite of ESN subsurface heat budget. As in Figure 6, but for composite of eight La Niña anomalies for the period 1979–2017 from CFSR reanalysis. Composite evolution of the heat budget anomalies are shown from June (0) to May (+1) centered on the peak winter months. All terms are in W/m^2.

After the peak warming in January (+1), the anomalous poleward flow weakens, turning equatorward, the zonal currents turn off-shore below the ML, and the downwelling motion also weakens thereby contributing to lessen the anomalous advective heating of the intermediate layer. The equatorward flow starts to drive the existing warmer waters through the southern boundary of the ESN resulting in anomalous cooling from March (+1) onwards.

3.2.2. La Niña Evolution

A composite of La Niña events (Figure 7) reveals anomalous cooling of the intermediate layer, as is expected, with the heat budget terms generally mirroring those during El Niño (compare Figures 6a and 7). It bears noting that our results are from a coarse resolution global climate model, which are notorious for very overly symmetric responses in El Niño versus La Niña. Figure 7 shows that during La Niña events, the intermediate layer anomalously cools from June (0) through March (+1), except for 2 months of warming in September (0) and October (0). The full field heat budget of the intermediate layer shows that the residual is a large heating term in the summers,

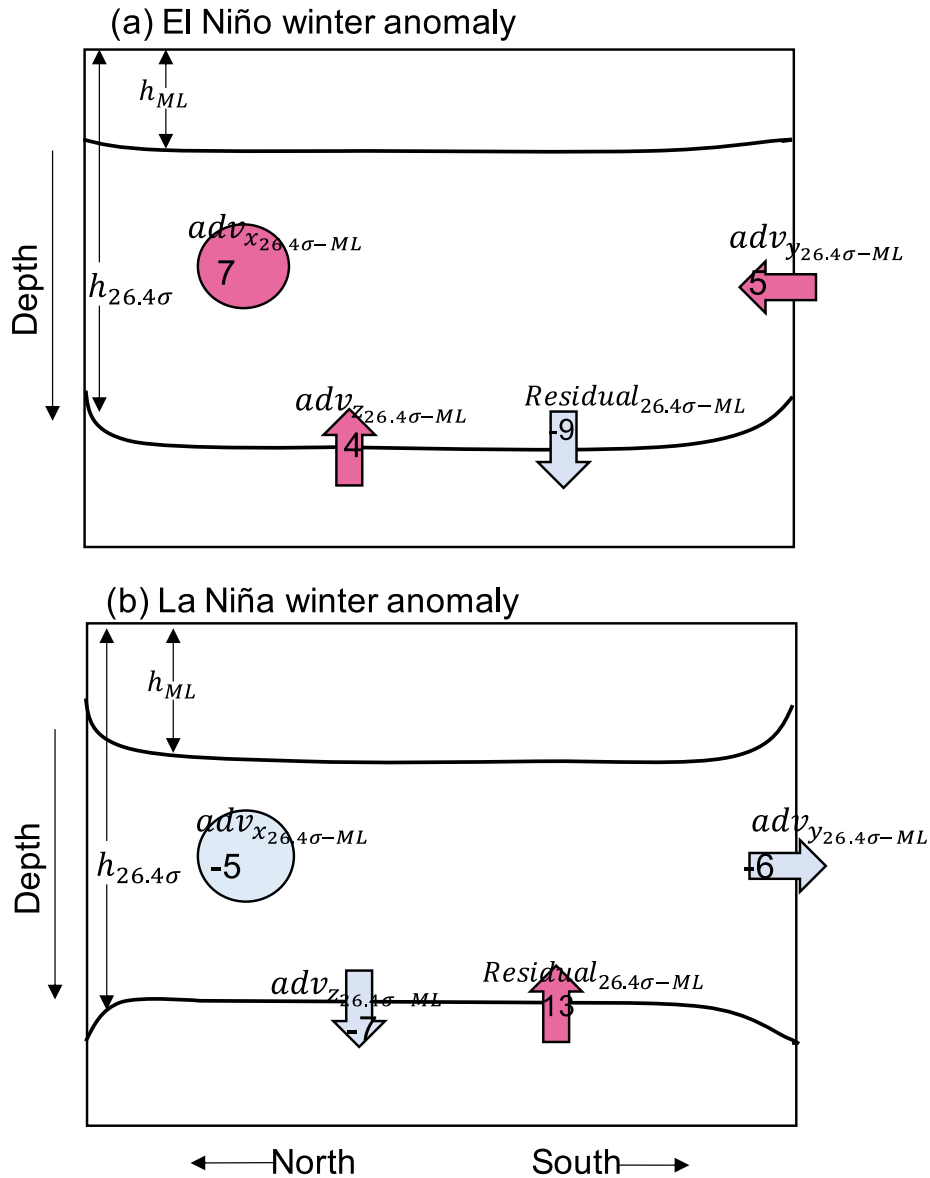

Figure 8. Schematic representation of the dominant fluxes in $HB_{26.4\sigma-ML}$ in ESN during ENSO. As in Figure 5, but for anomalous convergence and divergence of fluxes in $HB_{26.4\sigma-ML}$ during (a) El Niño and (b) La Niña in December. The numbers represent the average value in W/m^2 following Figures 6 and 7. The deepened mixed layer (h_{ML}) during La Niña winters in (b), and the deepening and shoaling of 26.4σ layer ($h_{26.4\sigma}$) during El Niño (a) and La Niña (b) winters are shown in black curves. The relatively thicker $h_{26.4\sigma}$–h_{ML} intermediate layer during El Niño winters is evident as seen from Figure A1. The convergence of *advx*, *advy*, and *advz* fluxes into this thicker layer drives the anomalous heating of the intermediate layer during El Niño. The opposite occurs in relatively thinner intermediate layer during La Niña winters. Note the heating from *Residual* during La Niña and cooling from *Residual* (reduced magnitude) during El Niño are in the opposite direction of the net heating/cooling.

when the intermediate layer is still warm (Figure A4). A decrease in residual heating seems to drive a reduced warming of the intermediate layer from September (0) to December (0) (Figure A4). The anomalous advective cooling picks up from October (0) onwards driving the strong cooling in intermediate layer (Figure 7). Unlike El Niño years, the residual heating in La Niña years continues until December (0), probably due to increased upper ocean mixing driving enhanced diffusive flux convergence below the ML (Figure A4). The peak cooling occurs in January (+1) when the intermediate layer is thinner than ENSO-neutral years by almost 10 m, due to a shoaling of the 26.4σ surface (Figure A1, Figure 8b). The shoaling of the bottom layer can be attributed in part to the passing of upwelling CTWs which are common during La Niña winters (Figure A1). The residual opposes

changes in the anomalous heat content of the intermediate layer due to advection much like as seen in the El Niño composites.

The decomposition of advection into its directional components reveals that all components contribute toward driving the anomalous cooling of the intermediate layer in La Niña winter. The brief warming during September (0)–October (0) is due primarily to the zonal and vertical advective components August (0) onward (Figure 7b). During this season of upwelling in La Niña years, the vertical circulation appears to be exporting relatively more cooler waters to the ML from above (in the ML) than importing from below (26.4σ layer) leading to a small anomalous heating from convergence of vertical advective fluxes in the intermediate layer, which persists till September (0). The strengthening of seasonal upwelling in the ML, also leads to increased onshore currents bringing in warmer off-shore waters in the intermediate layer below in the following months (October (0)–November (0)) through the western boundary of ESN (Figure A3). This leads to the anomalous zonal advective heating in these months in Figure 7. With the strengthening of equatorward current by October (0) the warmer intermediate layer waters are driven out through the southern boundary (Figure A2), which results in cooling from the meridional component October (0) onwards (Figure 7). The arrival of CTW, shoaling the 26.4σ layer from November (0) further enhances the existing upwelling conditions, with the vertical component driving the anomalous cooling along with zonal flux divergence. Thus at the peak of the event all the advective components have a similar sense in forcing anomalous cooling of the intermediate layer in December (0)–January (+1) (Figure 8b), much like the role they play in El Niño years. Although the evolution of the heat budget appears to be roughly opposite during El Niño and La Niña (Figures 6a and 7a) the processes driving the warming and cooling of the intermediate layer during the two types of events have differences only on considering the individual terms in the heat budget.

3.3. El Niño Minus La Niña Evolution

Poleward flow via the CUC and convergence of fluxes across ESN boundaries from downwelling of isopycnals results in greater heating of the intermediate layer during El Niño winters compared to that in La Niña winters. With a negligible role from surface fluxes, the difference in El Niño minus La Niña composites of ESN heat budget anomalies highlights a clear heating of the intermediate layer from advection, along with a cooling from residual of terms that include enhanced mixing during La Niña among other terms (sub-grid scale processes, submonthly processes, innovation terms). The representation of the dominant convergence (heating) and divergence (cooling) of fluxes in ENSO-neutral winters is shown in Figure 5, and that for El Niño and La Niña winters is shown in Figure 8.

Comparing Figures 6b–7b shows that although at the peak of the event the zonal component clearly is larger than other components in the advective heating in El Niño composites, such clear association to any particular component in La Niña composites is not evident. The associated deepening and shoaling of the 26.4σ layer (Figure A1) during the peak of El Niño and La Niña events demonstrates changes in isopycnal heave associated with ENSO and the propagation of CTWs. This results in thickening and thinning of the intermediate layer, respectively, along with the anomalous changes in vertical and zonal motion flux convergences as seen in the advection terms (Figure 8). High-resolution numerical ocean model simulations are liable to be required for a more complete diagnosis of the role(s) of fine-scale processes near the coast.

3.4. Relation Between Winter Advection and Subsurface Temperature Variations

The column mean winter advection is significantly correlated to the following summer temperatures within the 26.4σ layer, consistent with the results shown in Section 3.2.1 and Section 3.2.2. Figure 9 shows the correlations in the lag of averaged temperatures within ESN starting from October (Figure 9a), November (Figure 9b), December (Figure 9c) and January (Figure 9d) at all depths from surface to 300 m, to the advection ($advection_{26.4\sigma-ML}$) in October, November, December and January. The instantaneous correlations in the ML, and at times below the 26.4σ level, are generally higher than the correlations within the intermediate layer. In particular the correlations within this intermediate layer shows that advection in December-January (the peak in El Niño/La Niña composite) consistently explain higher percentage of temperature variance (36%) up to 6 months beyond, in comparison to the advection in October-November (decreases from 36% to 16% in 6 months). The anomalous convergence of advective fluxes during El Niño, and the anomalous divergence of advective fluxes during La Niña (Section 3.2.1 and Section 3.2.2) in December and January months play a key role in the temperature variations of the following

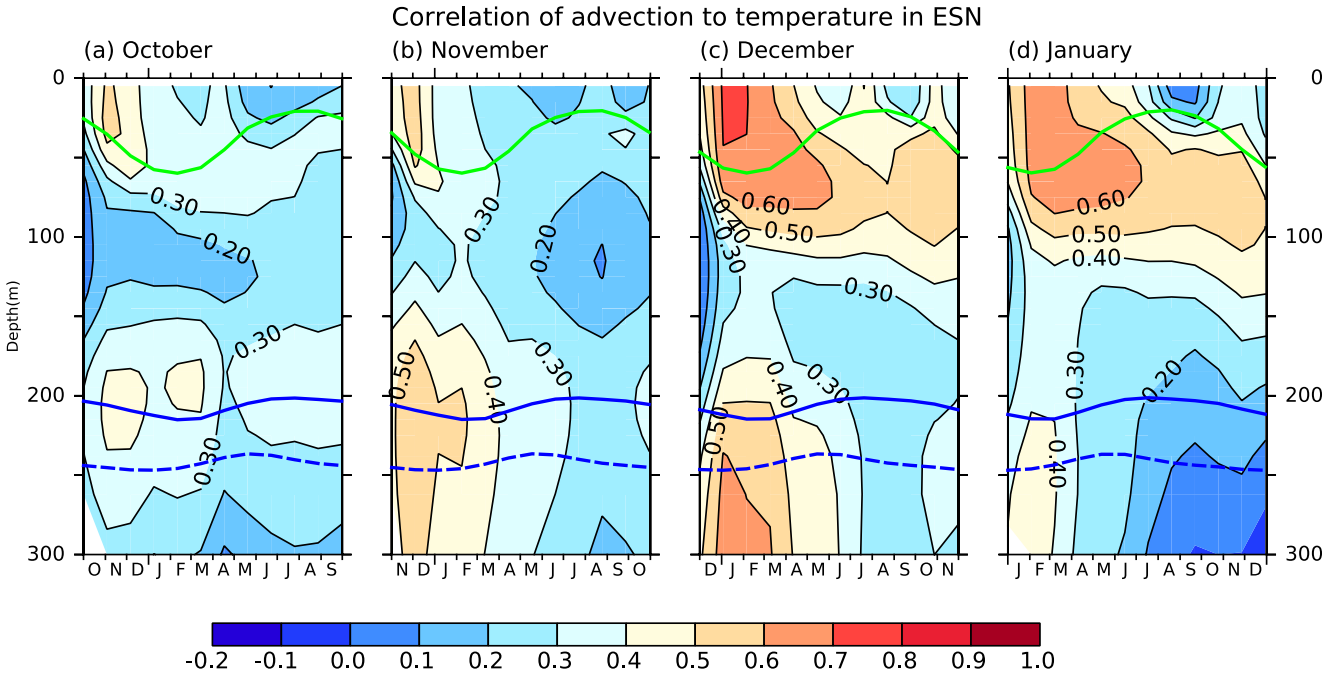

Figure 9. Lag correlation of ESN (128°W–122°W; 35°N–50°N) averaged potential temperature anomaly at each depth to averaged anomalous advection in the intermediate layer ($advection_{26.4\sigma-ML}$) in (a) October, (b) November, (c) December, and (d) January. Correlations are shaded and contoured in black. The ESN averaged climatological ML depth, and depth of 26.4σ level in green and blue, respectively. The climatological depth of 26.4σ averaged at the southern edge of the ESN region (35°*N*) is in blue dash.

summer (May–July) in ESN. And the downwelling/upwelling of isopycnals perhaps disrupts the local memory provided by winter advection prevalent during ENSO-neutral years.

4. Discussion

Subsurface temperature variations within the northern extent of the CCS (43°N−50°N) in winter are found to be significantly correlated to the following summer temperatures at 26.4σ level. Given the relevance of ecosystem impacts with conditions dependent on the prior season (Schroeder et al., 2013), a heat budget diagnostic is utilized to analyze relevant physical processes linking the summer to winter prior temperatures. Interannually, ENSO teleconnections are known to influence local processes within the CCS between 43°N and 50°N via atmospheric and oceanic pathways, notably CTW. A particular focus of our investigation is on drivers of winter subsurface temperatures during ENSO years to complement the large body of previous research showing how ENSO influences surface temperatures in the region. While winter mixing often explains the link between summer and winter prior temperatures, it fails to explain the subsurface temperature variations entirely between 43°N and 50°N (Figures 1 and 3). A heat budget for an intermediate layer is diagnosed on a monthly time scale to investigate the possible processes explaining such linkage.

Deep winter mixing is an important process driving seasonal subsurface variations in large parts of the North Pacific, but is only able to explain 25% of the temperature variability at the depth of 26.4σ in N-CCS (43°*N*−50°*N*) (Figure 3), with the remaining 75% attributable to a mix of local subsurface processes involving advection or mixing and remotely driven large-scale processes at different lags (Ray et al., 2020). The correlation between the net advective heat flux anomalies in winter in the intermediate layer to the following summer subsurface temperatures in the N-CCS (43°*N*−50°*N*) are as high as 36% (Figure 9). The strength of the correlation with the following summer temperatures is greatest for advection during December and January, when the advective heat fluxes are at their peak (Figures 6b and 7b). This is also the time of the year when the 26.4σ layer shows maximum deepening in association with El Niño and shoaling in association with La Niña as seen in Figure A1b,A1c. This supports our findings from the heat budget diagnosis as described below.

During ENSO-neutral periods, the total advective heat fluxes are minimal and drives the reduced heating of the intermediate layer from winter into spring. In contrast during summer, the residual consisting of vertical diffusive heat fluxes drives the intermediate layer heating. The meridional advection is a cooling effect year-round but is reduced with the appearance of seasonal CUC in November–March. The deepening of the 26.4σ layer during this downwelling season leads to convergence of fluxes in the vertical and zonal directions as well. However, the partial turning of meridional current poleward in the vicinity of the coast essentially reduces the cooling from meridional component into the intermediate layer in October-January, which pre-conditions the layer for the following summer and possibly leads to better correlations of the temperatures at 26.4σ depth (Figure 1). The subsurface poleward current weakens and turns equatorward from March-May, resulting in enhanced subsurface cooling of the intermediate layer.

During El Niño the poleward current represented by the CUC increases and along with the downwelling of isopycnals drives an anomalous convergence of advective fluxes, resulting in warming of the intermediate layer as summarized in Figure 8. An eddy like zonal recirculation pattern along western boundary of the ESN appears to form in the fall-winter season, consistent with observational and modeling evidence of eddies during El Niño (Di Lorenzo et al., 2005; Melsom et al., 2003; Murray et al., 2001). This feature causes zonal advective cooling, but is rapidly compensated in the following months by warmer waters from the south via the CUC. With the propagation of downwelling CTW and isopycnal heaving associated with El Niño, the 26.4σ layer is deepened and includes deeper layers of the CUC core. Our results are in agreement with Turi et al. (2018)'s study in a much higher resolution model with regard to deepening of isopycnals during El Niño and warmer waters being advected from the south. In addition our results also show that this deepened 26.4σ layer drives convergence of vertical and zonal advective fluxes in the intermediate layer. Thus an anomalous convergence of advective fluxes from all directions drives the peak winter months of El Niño (Figure 8). During La Niña years the seasonally strengthened upwelling plays a pre-conditioning role to the winter conditions. In an anomalously deeper winter ML enhanced upper ocean mixing increases convergence of diffusive heat flux below in the intermediate layer, as reflected by heating in the residual term. The anomalous increase in wind-driven upwelling at the same time also drive an anomalous on-shore current below the ML, driving in warmer waters across the western boundary in the ESN in the fall-winter transition months. However, with the arrival of upwelling CTW and vertical displacements in the isopycnals associated with La Niña, the subsurface circulation is dominated by an anomalous divergence of vertical and zonal advective fluxes. Along with an enhanced equatorward flow in the meridional direction, an anomalous divergence of all the fluxes drive the cooling in peak months during La Niña winters (Figure 8). The downward displacement of isopycnals seems to be more effective than upward displacement of isopycnals in confounding the local memory of the winter subsurface, as evident from weaker correlations during El Niño years compared to La Niña years (Section 2.4).

Diverse future projections from dynamically downscaled regional model simulations have highlighted the importance of understanding large-scale processes driving and interacting with coastal processes (Alexander et al., 2020; S. Siedlecki, Pilcher, et al., 2021). The linkages between the large-scale atmosphere-ocean climate system with coastal processes can be examined using either a computationally intensive global high resolution model (which can be impractical), or a dynamically downscaled regional model with large-scale boundary conditions from global climate models. Our study informs the second kind, in that knowing what processes dominate the subsurface in a global climate model paves the way for further analysis with a regional model. Such approach was used by Zaba et al. (2020) to diagnose the fine-scale coastal processes in a heat budget. Our analysis features considerations of (a) the large-scale circulation processes, (b) a temporally varying bottom depth of the heat budget domain that includes the effects of isopycnal heave, and also (c) accounts for the net heating or cooling of the enclosed domain from external influence of the advective fluxes (instead of redistributing heat internally). Unlike Zaba et al. (2020) our analysis did not include the innovation terms from data assimilation due to its unavailability, which contributes partially to the bigger residual term. But we do show that the residual, which is minimal in the winter season of particular interest to this study, accounts for the sense of the unresolved additional heating or cooling. Indeed, using only a few years and one reanalysis does result in some uncertainty; this study is an initial step to qualitatively demonstrate a subsurface heat budget in diagnosing processes driving subsurface temperatures of the N-CCS. Additionally, the present study demonstrates the potential in evaluating the effect of large-scale processes in coastal waters via this heat budget approach. Our reanalysis-based estimate of the heat budget indicates which terms are most important for the accurate prediction of subsurface temperatures in the

N-CCS. Although the potential predictability of summer temperatures at depth is suggested, hindcast experiments should be carried out with actual seasonal forecast experiments, such as J-SCOPE.

5. Conclusion

Oceanic advection (both horizontal and vertical) dominates the seasonal and interannual changes in temperature of the water column between a temporally varying ML and the 26.4σ level in the northern CCS (35°N–50°N). In this study we investigated the drivers of temperature changes in this intermediate layer. Using a reasonably closed heat budget a balance among advective components (zonal, meridional, and vertical) is found to be the primary driver of temperatures at depth during both ENSO and ENSO-neutral winters. The seasonal appearance of a near coastal poleward flow (CUC) in winter drives a shift in the meridional advection, which plays a leading role in pre-conditioning the winter subsurface for the following summer. The meridional component of advection is a particularly important term during ENSO-neutral winters; the vertical and zonal components are relatively important to the anomalous heating during El Niño and cooling during La Niña winters, respectively. In particular, the passing of remotely driven CTW and isopycnal heave associated with ENSO results in an anomalous deepening or shoaling of the 26.4σ layer that are accompanied by an anomalous convergence/divergence of vertical and zonal advective fluxes that disrupts the local memory prevalent during ENSO-neutral winters. This possibly explains the weaker correlations of winter temperatures at depth to those of the following summer, particularly following an El Niño year. A strengthened CUC during El Niño and inclusion of CUC core waters through a deepened 26.4σ layer drives an anomalous heating due to meridional advection. The advective flux anomalies are not symmetric to one another in El Niño versus La Niña years as evidenced by eddy-like recirculation driven cooling during El Niño fall-winter transitions only. We expect our results to provide guidance toward investigating sources of subsurface seasonal predictability in higher resolution coastal model frameworks.

Appendix A: Heat Budget of the Intermediate Layer

The layer depth h (h_{ML} and $h_{26.4\sigma}$) and the horizontal region together define the D and V_D ($V_{D_{ML}}$ and $V_{D_{26.4\sigma}}$) for the volume averages in Equation 1 (Figure A1, Figure A2, Figure A3, Figure A4). To compute HB_{ML}, and $HB_{26.4\sigma}$ we calculate the heat budget terms of each layer as below. For the layer depth $h = h_{ML}$, HB_{ML} in Equation 1 is

$$\partial_t T_{D_{ML}} = \frac{Q_{\text{sfc}_{ML}} - Q_{\text{pen}_{ML}}}{\rho_0 C_p V_{D_{ML}}} + \langle \text{advection}_{ML} \rangle + \langle \text{entrainment}_{ML} \rangle + \langle \text{residual}_{ML} \rangle$$

where,

$$\langle \text{advection}_{ML} \rangle = -\frac{1}{V_{D_{ML}}} \int_{S_{D_{ML}}} (\mathbf{u} \cdot \mathbf{n}) \left(T_{ML} - T_{D_{ML}} \right) dS = \langle \text{adv}_{x_{ML}} \rangle + \langle \text{adv}_{y_{ML}} \rangle + \langle \text{adv}_{z_{ML}} \rangle$$

$$\langle \text{entrainment}_{ML} \rangle = \frac{1}{V_{D_{ML}}} \iint_{S_{-h_{ML}}} \left(T_{-h_{ML}} - T_{D_{ML}} \right) \partial_t h_{ML} \; dx \; dy$$

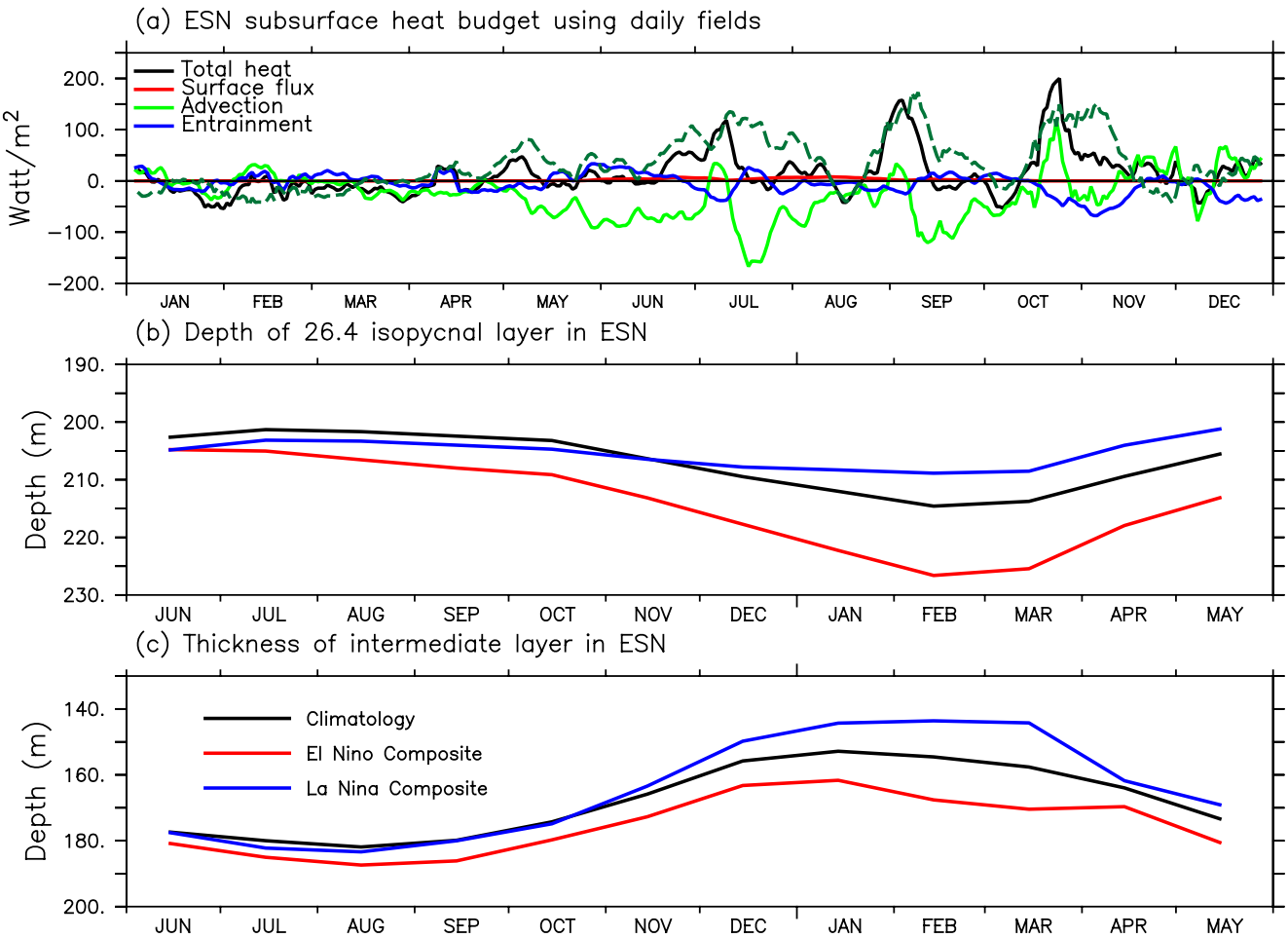

Figure A1. (a) Daily heat budget in CFSR. Evolution of daily heat budget terms for the year 1979—Total heat $\left(\sim T_{D_{26.4\sigma-ML}}\right)$, Surface flux heating $\left(\sim Q_{sfc_{26.4\sigma-ML}} - Q_{pen_{26.4\sigma-ML}}\right)$, heating from Advection $(\sim advection_{26.4\sigma-ML})$, Entrainment $(\sim entrainment_{26.4\sigma-ML})$ and the Residual (Residual$\sim Residual_{26.4\sigma-ML}$) in dash for the intermediate layer $(HB_{26.4\sigma-ML})$ within the Extended South N-CCS (ESN) domain. Heat budget terms in W/m^2 are calculated as in Appendix A. A boxcar smoothing over 7 days is applied on the daily time-series. Climatology, El Niño and La Niña composite of (b) monthly 26.4σ layer depth and (c) thickness of the intermediate layer (26.4σ−*ML*) from June to the following May for the period 1979 − 2017. All data are from CFSR reanalysis.

For the layer depth $h = h_{26.4\sigma}$, $HB_{26.4\sigma}$ in Equation 1 is

$$\partial_t T_{D_{26.4\sigma}} = \frac{Q_{\mathrm{sfc}_{26.4\sigma}} - Q_{\mathrm{pen}_{26.4\sigma}}}{\rho_0 C_p V_{D_{26.4\sigma}}} + \langle \mathrm{advection}_{26.4\sigma} \rangle + \langle \mathrm{entrainment}_{26.4\sigma} \rangle + \langle \mathrm{residual}_{26.4\sigma} \rangle$$

where,

$$\langle \mathrm{advection}_{26.4\sigma} \rangle = -\frac{1}{V_{D_{26.4\sigma}}} \int_{S_{D_{26.4\sigma}}} (\mathbf{u} \cdot \mathbf{n}) \left(T_{26.4\sigma} - T_{D_{26.4\sigma}} \right) dS = \langle \mathrm{adv}_{x_{26.4\sigma}} \rangle + \langle \mathrm{adv}_{y_{26.4\sigma}} \rangle + \langle \mathrm{adv}_{z_{26.4\sigma}} \rangle$$

$$\langle \mathrm{entrainment}_{26.4\sigma} \rangle = \frac{1}{V_{D_{26.4\sigma}}} \iint_{S_{-h_{26.4\sigma}}} \left(T_{-h_{26.4\sigma}} - T_{D_{26.4\sigma}} \right) \partial_t h_{26.4\sigma} \; dx \; dy$$

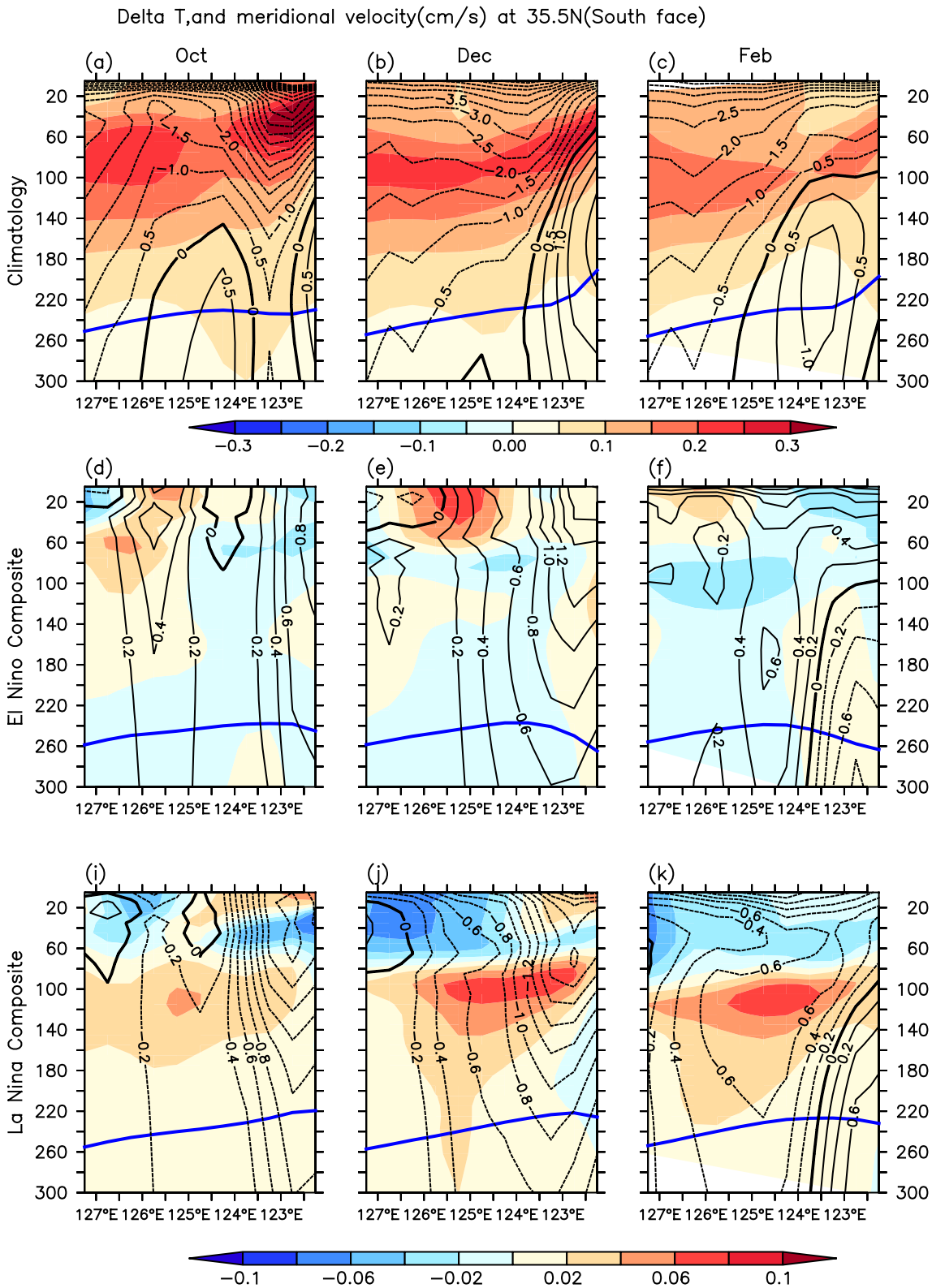

Figure A2. Climatology of (a)–(c) ΔT (shading) and v (contour, cm/sec) at the southern face of ESN (35.5°N) in (a) October, (b) December, and (c) February. The same but for the anomalies in (d)–(f) El Niño and (i)–(k) La Niña composites. In each figure the depth of 26.4σ layer is shown in blue line. ΔT is the difference in temperature at the southern edge of each grid minus the grid temperature, instead of the T–T_D used to calculate in heat budget calculations. The deepening/shoaling of the 26.4σ close to the coast during El Niño/La Niña is visible in (d)–(f)/(i)–(k).

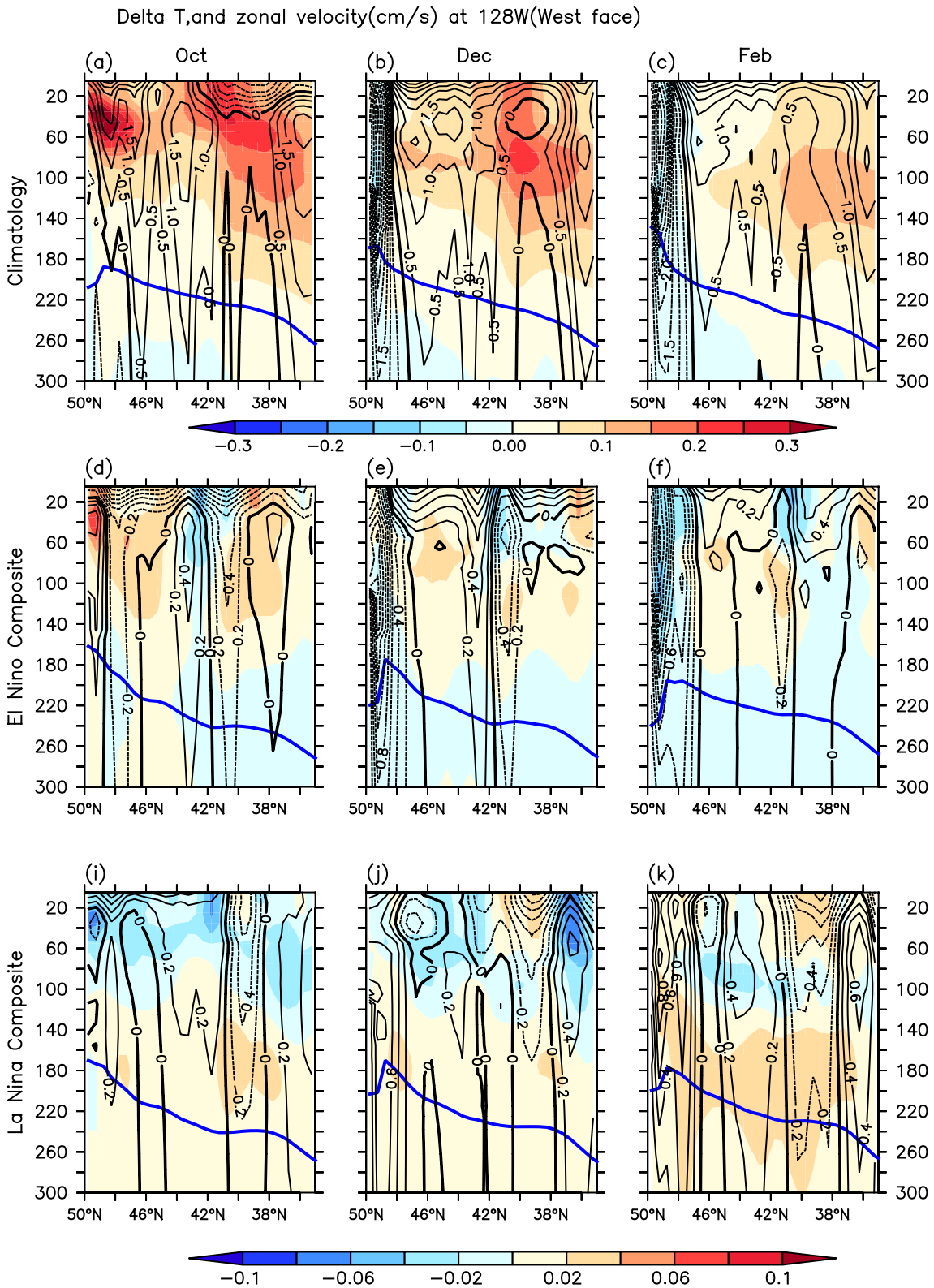

Figure A3. As in Figure A2 but for ΔT (shading) and u (contour, cm/sec) at the western face of ESN (128°N). The latitudinal slope in 26.4σ layer with deepening toward south and shoaling northward is visible.

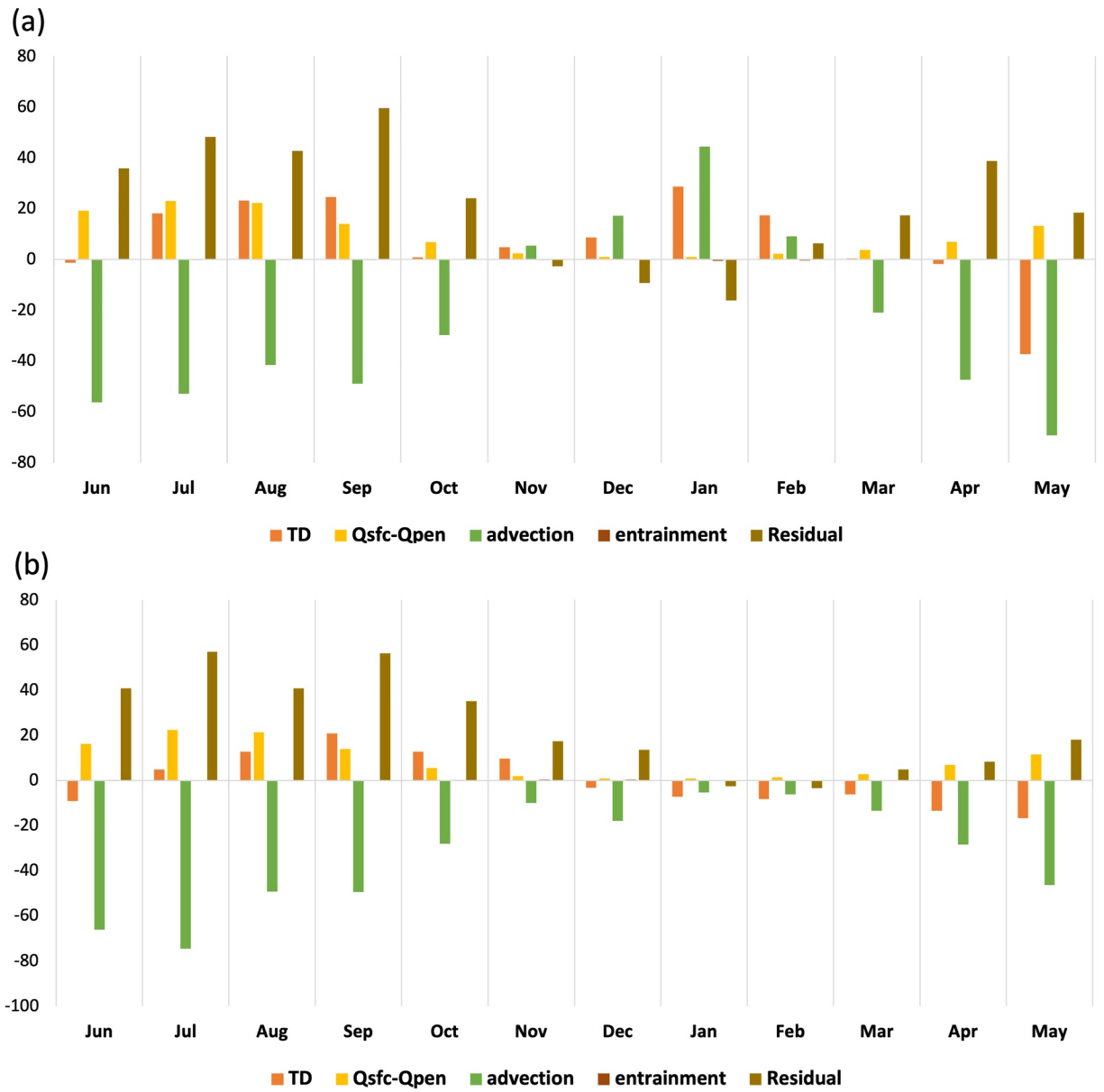

Figure A4. ENSO composite heat budget. Evolution of ESN heat budget ($HB_{26.4\sigma-ML}$) in (a) El Niño, and (b) La Niña composites. As in Figure 4, but for the composites of full fields. All terms are in W/m^2. Data used is for the period 1979–2017.

The intermediate layer budget, $HB_{26.4\sigma-ML}$ is then

$$\partial_t T_{D_{26.4\sigma}} - \partial_t T_{D_{ML}} = \left(\frac{Q_{\text{sfc}_{26.4\sigma}}}{\rho_0 C_p V_{D_{26.4\sigma}}} - \frac{Q_{\text{sfc}_{ML}}}{\rho_0 C_p V_{D_{\text{ML}}}}\right) + \left(\frac{Q_{\text{pen}_{ML}}}{\rho_0 C_p V_{D_{\text{ML}}}} - \frac{Q_{\text{pen}_{26.4\sigma}}}{\rho_0 C_p V_{D_{26.4\sigma}}}\right) + (\langle \text{advection}_{26.4\sigma}\rangle - \langle \text{advection}_{ML}\rangle) + (\langle \text{entrainment}_{26.4\sigma}\rangle - \langle \text{entrainment}_{ML}\rangle) + (\langle \text{residual}_{26.4\sigma}\rangle - \langle \text{residual}_{ML}\rangle)$$

where the individual terms represented are

$$\frac{Q_{\text{sfc}_{26.4\sigma}}}{\rho_0 C_p V_{D_{26.4\sigma}}} - \frac{Q_{\text{sfc}_{ML}}}{\rho_0 C_p V_{D_{\text{ML}}}} \equiv Net\ Surface_{26.4\sigma-ML}$$

$$\frac{Q_{\mathrm{pen}_{ML}}}{\rho_0 C_p V_{D_{\mathrm{ML}}}} - \frac{Q_{\mathrm{pen}_{26.4\sigma}}}{\rho_0 C_p V_{D_{26.4\sigma}}} \equiv Shortwave\ Penetration_{26.4\sigma-ML}$$

$$\begin{aligned}\langle \mathrm{advection}_{26.4\sigma}\rangle - \langle \mathrm{advection}_{ML}\rangle &= \left(\langle \mathrm{adv}_{x_{26.4\sigma}}\rangle - \langle \mathrm{adv}_{x_{ML}}\rangle\right) + \left(\langle \mathrm{adv}_{y_{26.4\sigma}}\rangle - \langle \mathrm{adv}_{y_{ML}}\rangle\right) \\ &\quad + \left(\langle \mathrm{adv}_{z_{26.4\sigma}}\rangle - \langle \mathrm{adv}_{z_{ML}}\rangle\right) \\ &\equiv \langle \mathrm{adv}_{x_{26.4\sigma-ML}}\rangle + \langle \mathrm{adv}_{y_{26.4\sigma-ML}}\rangle + \langle \mathrm{adv}_{z_{26.4\sigma-ML}}\rangle\end{aligned}$$

$$\begin{aligned}\langle \mathrm{entrainment}_{26.4\sigma}\rangle - \langle \mathrm{entrainment}_{ML}\rangle &= \frac{1}{V_{D_{26.4\sigma}}} \iint_{S_{-h_{26.4\sigma}}} \left(T_{-h_{26.4\sigma}} - T_{D_{26.4\sigma}}\right) \partial_t h_{26.4\sigma}\ dx\ dy \\ &\quad - \frac{1}{V_{D_{ML}}} \iint_{S_{-h_{ML}}} \left(T_{-h_{ML}} - T_{D_{ML}}\right) \partial_t h_{ML}\ dx\ dy \\ &\equiv Entrainment_{26.4\sigma-ML}\end{aligned}$$

$$\langle \mathrm{residual}_{26.4\sigma}\rangle - \langle \mathrm{residual}_{ML}\rangle = Residual_{26.4\sigma-ML}$$

Data Availability Statement

CFSR datasets for analysis were obtained from https://www.ncei.noaa.gov/products/weather-climate-models/climate-forecast-system.

Acknowledgments
We thank the reviewers for their constructive comments in improving the paper. We acknowledge the insights provided by Andrew Wittenberg of NOAA/GFDL with regards to constructing a heat budget and interpreting its results. This study was supported by NOAA's Climate Program Office's Modeling, Analysis, Predictions, and Projections Program, Grant NA17OAR4310112. Computations were done on the University of Connecticut HPC Storrs Cluster supercomputer system.

References

Aalto, E., Lafferty, K. D., Sokolow, S., Grewelle, R., Ben-Horin, T., Boch, C., et al. (2020). Models with environmental drivers offer a plausible mechanism for the rapid spread of infectious disease outbreaks in marine organisms. *Scientific Reports*, *10*(1), 1–10. https://doi.org/10.1038/s41598-020-62118-4

Alexander, M. A., Deser, C., & Timlin, M. S. (1999). The reemergence of SST anomalies in the north Pacific ocean. *Journal of Climate*, *12*(8), 2419–2433. https://doi.org/10.1175/1520-0442(1999)012<2419:trosai>2.0.co;2

Alexander, M. A., Scott, J. D., Friedland, K. D., Mills, K. E., Nye, J. A., Pershing, A. J., et al. (2018). Projected sea surface temperatures over the 21st century: Changes in the mean, variability and extremes for large marine ecosystem regions of northern oceans. *Elementa: Science of the Anthropocene*, *6*. https://doi.org/10.1525/elementa.191

Alexander, M. A., Shin, S.-i., Scott, J. D., Curchitser, E., & Stock, C. (2020). The response of the northwest Atlantic Ocean to climate change. *Journal of Climate*, *33*(2), 405–428. https://doi.org/10.1175/jcli-d-19-0117.1

Amaya, D. J., Jacox, M. G., Dias, J., Alexander, M. A., Karnauskas, K. B., Scott, J. D., & Gehne, M. (2022). Subseasonal-to-seasonal forecast skill in the California current system and its connection to coastal kelvin waves. *Journal of Geophysical Research: Oceans*, *127*(1), e2021JC017892. https://doi.org/10.1029/2021jc017892

Amaya, D. J., Miller, A. J., Xie, S.-P., & Kosaka, Y. (2020). Physical drivers of the summer 2019 north Pacific marine heatwave. *Nature Communications*, *11*(1), 1–9. https://doi.org/10.1038/s41467-020-15820-w

Bamston, A. G., Chelliah, M., & Goldenberg, S. B. (1997). Documentation of a highly ENSO-related SST region in the equatorial Pacific: Research note. *Atmosphere-Ocean*, *35*(3), 367–383. https://doi.org/10.1080/07055900.1997.9649597

Bond, N. A., Cronin, M. F., Freeland, H., & Mantua, N. (2015). Causes and impacts of the 2014 warm anomaly in the ne Pacific. *Geophysical Research Letters*, *42*(9), 3414–3420. https://doi.org/10.1002/2015gl063306

Brickman, D., Alexander, M. A., Pershing, A., Scott, J. D., & Wang, Z. (2021). Projections of physical conditions in the Gulf of Maine in 2050. *Elementa: Science of the Anthropocene*, *9*(1), 00055. https://doi.org/10.1525/elementa.2020.20.00055

Byju, P., Dommenget, D., & Alexander, M. (2018). Widespread reemergence of sea surface temperature anomalies in the global oceans, including tropical regions forced by reemerging winds. *Geophysical Research Letters*, *45*(15), 7683–7691. https://doi.org/10.1029/2018gl079137

Chen, K., Gawarkiewicz, G., Kwon, Y.-O., & Zhang, W. G. (2015). The role of atmospheric forcing versus ocean advection during the extreme warming of the northeast us continental shelf in 2012. *Journal of Geophysical Research: Oceans*, *120*(6), 4324–4339. https://doi.org/10.1002/2014jc010547

Chen, K., Kwon, Y.-O., & Gawarkiewicz, G. (2016). Interannual variability of winter-spring temperature in the middle Atlantic bight: Relative contributions of atmospheric and oceanic processes. *Journal of Geophysical Research: Oceans*, *121*(6), 4209–4227. https://doi.org/10.1002/2016jc011646

Cimino, M. A., Santora, J. A., Schroeder, I., Sydeman, W., Jacox, M. G., Hazen, E. L., & Bograd, S. J. (2020). Essential krill species habitat resolved by seasonal upwelling and ocean circulation models within the large marine ecosystem of the California current system. *Ecography*, *43*(10), 1536–1549. https://doi.org/10.1111/ecog.05204

Di Lorenzo, E., Foreman, M., & Crawford, W. (2005). Modelling the generation of Haida eddies. *Deep Sea Research Part II: Topical Studies in Oceanography*, *52*(7–8), 853–873. https://doi.org/10.1016/j.dsr2.2005.02.007

Di Lorenzo, E., & Mantua, N. (2016). Multi-year persistence of the 2014/15 north Pacific marine heatwave. *Nature Climate Change*, *6*(11), 1042–1047. https://doi.org/10.1038/nclimate3082

Di Lorenzo, E., Schneider, N., Cobb, K. M., Franks, P., Chhak, K., Miller, A. J., et al. (2008). North Pacific gyre oscillation links ocean climate and ecosystem change. *Geophysical Research Letters*, *35*(8), L08607. https://doi.org/10.1029/2007gl032838

Ding, H., Alexander, M. A., & Jacox, M. G. (2021). Role of geostrophic currents in future changes of coastal upwelling in the California current system. *Geophysical Research Letters*, *48*(3), e2020GL090768. https://doi.org/10.1029/2020gl090768

Fewings, M. R., & Brown, K. S. (2019). Regional structure in the marine heat wave of summer 2015 off the Western United States. *Frontiers in Marine Science*, *6*, 564. https://doi.org/10.3389/fmars.2019.00564

Frölicher, T. L., Fischer, E. M., & Gruber, N. (2018). Marine heatwaves under global warming. *Nature*, *560*(7718), 360–364. https://doi.org/10.1038/s41586-018-0383-9

Fumo, J. T., Carter, M. L., Flick, R. E., Rasmussen, L. L., Rudnick, D. L., & Iacobellis, S. F. (2020). Contextualizing marine heatwaves in the southern California bight under anthropogenic climate change. *Journal of Geophysical Research: Oceans*, *125*(5), e2019JC015674. https://doi.org/10.1029/2019jc015674

Jacox, M. G., Alexander, M. A., Siedlecki, S., Chen, K., Kwon, Y.-O., Brodie, S., et al. (2020). Seasonal-to-interannual prediction of north American coastal marine ecosystems: Forecast methods, mechanisms of predictability, and priority developments. *Progress in Oceanography*, *183*, 102307. https://doi.org/10.1016/j.pocean.2020.102307

Kwiatkowski, L., Torres, O., Bopp, L., Aumont, O., Chamberlain, M., Christian, J. R., et al. (2020). Twenty-first century ocean warming, acidification, deoxygenation, and upper-ocean nutrient and primary production decline from CMIP6 model projections. *Biogeosciences*, *17*(13), 3439–3470. https://doi.org/10.5194/bg-17-3439-2020

Lilly, L. E., & Ohman, M. D. (2021). Euphausiid spatial displacements and habitat shifts in the southern California current system in response to El Niño variability. *Progress in Oceanography*, *193*, 102544. https://doi.org/10.1016/j.pocean.2021.102544

Litzow, M. A., Hunsicker, M. E., Bond, N. A., Burke, B. J., Cunningham, C. J., Gosselin, J. L., et al. (2020). The changing physical and ecological meanings of north Pacific ocean climate indices. *Proceedings of the National Academy of Sciences*, *117*(14), 7665–7671. https://doi.org/10.1073/pnas.1921266117

Malick, M. J., Hunsicker, M. E., Haltuch, M. A., Parker-Stetter, S. L., Berger, A. M., & Marshall, K. N. (2020). Relationships between temperature and Pacific hake distribution vary across latitude and life-history stage. *Marine Ecology Progress Series*, *639*, 185–197. https://doi.org/10.3354/meps13286

McCabe, R. M., Hickey, B. M., Kudela, R. M., Lefebvre, K. A., Adams, N. G., Bill, B. D., et al. (2016). An unprecedented coast wide toxic algal bloom linked to anomalous ocean conditions. *Geophysical Research Letters*, *43*(19), 10–366. https://doi.org/10.1002/2016gl070023

Melsom, A., Metzger, E. J., & Hurlburt, H. E. (2003). Impact of remote oceanic forcing on gulf of Alaska sea levels and mesoscale circulation. *Journal of Geophysical Research*, *108*(C11), 3346. https://doi.org/10.1029/2002jc001742

Murray, C. P., Morey, S. L., & O'Brien, J. J. (2001). Interannual variability of upper ocean vorticity balances in the gulf of Alaska. *Journal of Geophysical Research*, *106*(C3), 4479–4491. https://doi.org/10.1029/1999jc000071

NOAA. (2022). Cold and warm episodes by season. Retrieved from https://origin.cpc.ncep.noaa.gov/products/analysis_monitoring/ensostuff/ONI_v5.php

Oliver, E. C., Burrows, M. T., Donat, M. G., Sen Gupta, A., Alexander, L. V., Perkins-Kirkpatrick, S. E., et al. (2019). Projected marine heatwaves in the 21st century and the potential for ecological impact. *Frontiers in Marine Science*, *6*, 734. https://doi.org/10.3389/fmars.2019.00734

Paulson, C. A., & Simpson, J. J. (1977). Irradiance measurements in the upper ocean. *Journal of Physical Oceanography*, *7*(6), 952–956. https://doi.org/10.1175/1520-0485(1977)007<0952:imituo>2.0.co;2

Peterson, W. T., Fisher, J. L., Strub, P. T., Du, X., Risien, C., Peterson, J., & Shaw, C. T. (2017). The pelagic ecosystem in the northern California current off Oregon during the 2014–2016 warm anomalies within the context of the past 20 years. *Journal of Geophysical Research: Oceans*, *122*(9), 7267–7290. https://doi.org/10.1002/2017jc012952

Rasmussen, L. L., Carter, M. L., Flick, R. E., Hilbern, M., Fumo, J. T., Cornuelle, B. D., et al. (2020). A century of southern California coastal ocean temperature measurements. *Journal of Geophysical Research: Oceans*, *125*(5), e2019JC015673. https://doi.org/10.1029/2019jc015673

Ray, S., Siedlecki, S., Alexander, M., Bond, N., & Hermann, A. (2020). Drivers of subsurface temperature variability in the northern California current. *Journal of Geophysical Research: Oceans*, *125*(8), e2020JC016227. https://doi.org/10.1029/2020jc016227

Ray, S., Wittenberg, A. T., Griffies, S. M., & Zeng, F. (2018). Understanding the equatorial Pacific cold tongue time-mean heat budget. Part I: Diagnostic framework. *Journal of Climate*, *31*(24), 9965–9985. https://doi.org/10.1175/jcli-d-18-0152.1

Ren, A. S., & Rudnick, D. L. (2021). Temperature and salinity extremes from 2014-2019 in the California current system and its source waters. *Communications Earth & Environment*, *2*(1), 1–9. https://doi.org/10.1038/s43247-021-00131-9

Rogers-Bennett, L., & Catton, C. (2019). Marine heat wave and multiple stressors tip bull kelp forest to sea urchin barrens. *Scientific Reports*, *9*(1), 1–9. https://doi.org/10.1038/s41598-019-51114-y

Rudnick, D. L., Zaba, K. D., Todd, R. E., & Davis, R. E. (2017). A climatology of the California current system from a network of underwater gliders. *Progress in Oceanography*, *154*, 64–106. https://doi.org/10.1016/j.pocean.2017.03.002

Ryan, J., Kudela, R., Birch, J., Blum, M., Bowers, H., Chavez, F., et al. (2017). Causality of an extreme harmful algal bloom in Monterey bay, California, during the 2014–2016 northeast Pacific warm anomaly. *Geophysical Research Letters*, *44*(11), 5571–5579. https://doi.org/10.1002/2017gl072637

Saha, S., Moorthi, S., Pan, H.-L., Wu, X., Wang, J., Nadiga, S., et al. (2010). The NCEP climate forecast system reanalysis. *Bulletin of the American Meteorological Society*, *91*(8), 1015–1058. https://doi.org/10.1175/2010bams3001.1

Sanford, E., Sones, J. L., García-Reyes, M., Goddard, J. H., & Largier, J. L. (2019). Widespread shifts in the coastal biota of northern California during the 2014–2016 marine heatwaves. *Scientific Reports*, *9*(1), 1–14. https://doi.org/10.1038/s41598-019-40784-3

Scannell, H. A., Johnson, G. C., Thompson, L., Lyman, J. M., & Riser, S. C. (2020). Subsurface evolution and persistence of marine heatwaves in the northeast Pacific. *Geophysical Research Letters*, *47*(23), e2020GL090548. https://doi.org/10.1029/2020gl090548

Schmidt, J. O., Bograd, S. J., Arrizabalaga, H., Azevedo, J. L., Barbeaux, S. J., Barth, J. A., et al. (2019). Future ocean observations to connect climate, fisheries and marine ecosystems. *Frontiers in Marine Science*, *6*, 550. https://doi.org/10.3389/fmars.2019.00550

Schroeder, I. D., Black, B. A., Sydeman, W. J., Bograd, S. J., Hazen, E. L., Santora, J. A., & Wells, B. K. (2013). The north Pacific high and wintertime pre-conditioning of California current productivity. *Geophysical Research Letters*, *40*(3), 541–546. https://doi.org/10.1002/grl.50100

Siedlecki, S., Salisbury, J., Gledhill, D., Bastidas, C., Meseck, S., McGarry, K., et al. (2021). Projecting ocean acidification impacts for the gulf of Maine to 2050: New tools and expectations. *Elementa: Science of the Anthropocene*, *9*(1), 00062. https://doi.org/10.1525/elementa.2020.00062

Siedlecki, S. A., Kaplan, I. C., Hermann, A. J., Nguyen, T. T., Bond, N. A., Newton, J. A., et al. (2016). Experiments with seasonal forecasts of ocean conditions for the northern region of the California current upwelling system. *Scientific Reports*, *6*(1), 1–18. https://doi.org/10.1038/srep27203

Siedlecki, S. A., Pilcher, D., Howard, E. M., Deutsch, C., MacCready, P., Norton, E. L., et al. (2021). Coastal processes modify projections of some climate-driven stressors in the California current system. *Biogeosciences*, *18*(9), 2871–2890. https://doi.org/10.5194/bg-18-2871-2021

Suryan, R. M., Arimitsu, M. L., Coletti, H. A., Hopcroft, R. R., Lindeberg, M. R., Barbeaux, S. J., et al. (2021). Ecosystem response persists after a prolonged marine heatwave. *Scientific Reports*, *11*(1), 1–17. https://doi.org/10.1038/s41598-021-83818-5

Testor, P., De Young, B., Rudnick, D. L., Glenn, S., Hayes, D., Lee, C. M., et al. (2019). Oceangliders: A component of the integrated goos. *Frontiers in Marine Science*, *6*, 422. https://doi.org/10.3389/fmars.2019.00422

Turi, G., Alexander, M., Lovenduski, N. S., Capotondi, A., Scott, J., Stock, C., et al. (2018). Response of o 2 and pH to ENSO in the California current system in a high-resolution global climate model. *Ocean Science*, *14*(1), 69–86. https://doi.org/10.5194/os-14-69-2018

Wei, X., Li, K.-Y., Kilpatrick, T., Wang, M., & Xie, S.-P. (2021). Large-scale conditions for the record-setting southern California marine heatwave of august 2018. *Geophysical Research Letters*, *48*(7), e2020GL091803. https://doi.org/10.1029/2020gl091803

Zaba, K. D., Rudnick, D. L., Cornuelle, B. D., Gopalakrishnan, G., & Mazloff, M. R. (2020). Volume and heat budgets in the coastal California current system: Means, annual cycles, and interannual anomalies of 2014–16. *Journal of Physical Oceanography*, *50*(5), 1435–1453. https://doi.org/10.1175/jpo-d-19-0271.1